A 'stack' model of rate-independent polycrystals

M Arul Kumar [a] Sivasambu Mahesh [a,b] P. Venkitanarayanan [a]

[a] *Department of Mechanical Engineering, Indian Institute of Technology, Kanpur 208016. India.*

[b] *Department of Aerospace Engineering, Indian Institute of Technology, Kanpur 208016. India.*

Abstract

A novel 'stack' model of a rate-independent polycrystal, which extends the 'ALAMEL' model of Van Houtte et al. (2005) is proposed. In the 'stack' model, stacks of N neighboring 'ALAMEL' domains collectively accommodate the imposed macroscopic deformation while deforming such that velocity and traction continuity with their neighbors is maintained. The flow law and consistency conditions are derived and an efficient solution methodology based on the linear programming technique is given. The present model is applied to study plastic deformation of an idealized two-dimensional polycrystal under macroscopically imposed plane-strain tension and simple shear constraints. Qualitative and quantitative variations in the predicted macroscopic and microscopic response with N are presented. The constraint on individual 'ALAMEL' domains diminishes with stack size N but saturates for large N. Computational effort associated with the present model is analyzed and found to be well within one order of magnitude greater than that required to solve the classical Taylor model. Furthermore, implementation of the consistency conditions is found to reduce computation time by at least 50%.

Preprint submitted to Elsevier Science *1 November 2010*

Key words: crystal plasticity, polycrystal model, flow law, consistency conditions, linear programming

---

* Corresponding author
Email address: smahesh@iitk.ac.in (Sivasambu Mahesh).

1 Introduction

In numerical simulations of polycrystal plastic deformation (Mathur and Dawson, 1989, Beaudoin et al., 1993, 1995, Mika and Dawson, 1998, Barbe et al., 2001, Ganapathysubramanian and Zabaras, 2005, Logé and Chastel, 2006, Van Houtte et al., 2006, Guan et al., 2006, Haddadi et al., 2006, Amirkhizi and Nemat-Nasser, 2007, Barton et al., 2008), microstructure-based prediction of material point response offer advantages over phenomenology-based predictions (Kim et al., 2008, Wang et al., 2008, Van Houtte et al., 2009, and references therein), albeit at greater computational cost. One advantage is that microstructure-based methods are applicable without restrictions for all loading histories, and also typically over a wider range of strain-rates and temperatures than phenomenological methods. Also, microstructure-based models predict material response at both macro- and micro-scales. They are therefore amenable to experimental verification at both scales (Peeters et al., 2001b,a, Mahesh et al., 2004).

Microstructure-based polycrystal plasticity models evolve the lattice orientation and anisotropic hardening of grains in response to macroscopically imposed constraints on the material point. A number of microstructure-based models are presently available. These range from the simple, yet qualitatively successful Taylor model (Taylor, 1938, Hirsch and Lucke, 1988a,b) to the crystal plasticity finite element method (Kalidindi et al., 1992, Kalidindi and Duvvuru, 2005, Kalidindi et al., 2006, Knezevic et al., 2008). While the former assumes that each grain of the polycrystal deforms according to the macroscopic constraint (Taylor hypothesis), the latter resolves spatial variations of deformation down to the sub-granular scale. The greater resolution

comes at a cost: Computationally, the former is typically two to three orders of magnitude less expensive than the latter. Since most of the computational expense of numerical simulations of macroscopic processes implementing microstructure-based material models is incurred during microstructure-level computations (Barton et al., 2008), and since the Taylor model is computationally the lightest model available, it has been the method of choice for microstructure-based material response prediction in macroscopic numerical simulations (e.g., Mathur and Dawson (1989), Beaudoin et al. (1993)).

However, it is now recognized that a quantitatively imprecise model for the evolution of the microstructure can be more deleterious to the accuracy of the macroscopic predictions than a phenomenological model, or a model of the microstructure that does not evolve with deformation (Van Houtte et al., 2005). The Taylor model, although qualitatively successful in predicting texture evolution has several shortcomings such as its tendency to overestimate texturing rate, its inability to predict the formation of certain experimentally observed texture components, its unsuitability in sub-structural studies, its inability to model intragranular phenomena, and its inapplicability to low symmetry materials (Leffers, 1975, Leffers and Christoffersen, 1997, Leffers, 1978, Hirsch and Lucke, 1988a,b, Christoffersen and Leffers, 1997, Mika and Dawson, 1998). Much recent effort has therefore focused on developing modifications of the Taylor model that, on the one hand, preserve its computational lightness, and on the other hand, render its microstructural predictions quantitatively accurate.

Successful approaches to modifying the Taylor model invariably hinge upon better approximations of the stress in a grain (Leffers, 1978, Aernoudt et al., 1993). In perhaps the earliest such approach Honneff and Mecking (1978) re-

laxed rolling direction shear constraints in rolling simulations by setting the corresponding shear tractions to zero. They found that this reduced the rate of texturing and led to better comparison between the predicted and experimental textures. The mixed deformation-rate and traction boundary condition of Honneff and Mecking (1978), developed further by Kocks and Canova (1981), Kocks and Chandra (1982), Van Houtte (1982), Christoffersen and Leffers (1997) is known as relaxed constraints. It differs from full constraints wherein all components of the deformation-rate are imposed upon a grain. Relaxed and full constraints are ideally suited when the granular morphology is pancake shaped and equiaxed, respectively. Tomé et al. (1984) have provided a technique to effect a transition from full to relaxed constraints with increasing grain aspect ratio.

Although constraint relaxation reduces the texturing rate during plane strain deformation, it too fails to quantitatively match the experimental texture evolution (Van Houtte et al., 1999). This failure is ascribed to the neglect of inter-granular interactions in Taylor-like models. As a first-order correction, pairwise interaction between neighboring grains has been incorporated into the polycrystal model. This interaction takes the form of velocity and traction continuity between neighboring grains. Depending on whether individual grains are taken to deform homogeneously or otherwise, the continuity conditions vary between two limiting forms. If inhomogeneous deformation of grains is permitted, geometrically necessary dislocations, proposed by Ashby (1970) will be generated within individual grains and accommodate any misfits between the grains. If the energy stored in the geometrically necessary dislocations is taken to be negligible, arbitrary misfits could be accommodated by them. This corresponds to the case of Leffers (1975), wherein only trac-

tion continuity between interacting grains is enforced. This limit will be called the $\mathscr{S}$-type continuity condition below. The other limit, called the $\mathscr{E}$-type continuity condition results when the energy penalty associated with the geometrically necessary dislocations accommodating misfits between neighboring grains is very large. In this case, each grain must deform homogeneously and compatibly with the other; the only role of geometrically necessary dislocations, confined to the grain boundary, is to rotate the grains such that voids or interpenetrations are avoided at the grain boundary (Ashby, 1970). Traction continuity between the grains must also be preserved.

The $\mathscr{E}$-type condition, which enforces velocity and traction continuity across a grain boundary, has been employed extensively to model pairwise intergranular interactions. Thus, within the self-consistent framework of Molinari et al. (1987) and Lebensohn and Tomé (1993), interaction equations for a grain with the surrounding homogeneous effective medium were developed by Lebensohn et al. (1998a) and Lebensohn (1999) for a grain comprised of codeforming matrix and twin regions. The models of Lee et al. (2002) and Van Houtte et al. (1999, 2005) disregard the self-consistent hypothesis and treat the polycrystal as a collection of bicrystals. Each bicrystal in these models satisfies the Taylor hypothesis, i.e., accommodates the imposed macroscopic constraints by codeformation of its two constituent grains.

The models described above have been extended to include more than pairwise interactions between grains. The self-consistent interaction equation derived by Garmestani et al. (2001) extends the model of Lebensohn et al. (1998b) and Lebensohn (1999). It considers inter-granular interaction through two- or three-point correlation functions of lattice orientations. Similarly, the rate-dependent and rate-independent binary-tree based models of Mahesh (2009,

2010) extend the models of Lee et al. (2002) and Van Houtte et al. (1999, 2005) to multi-grain interactions.

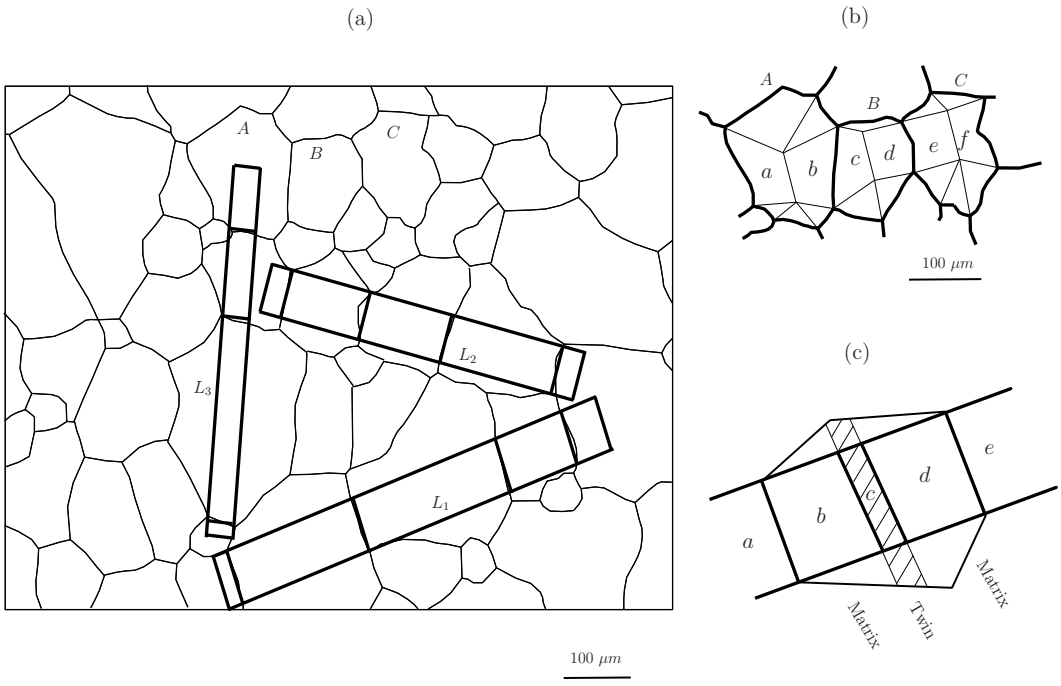

Fig. 1. Development of the 'stack' model from a 2-D microstructure (Manonukul and Dunne, 2004). (a) Microstructure showing the three largest stacks, L_1, L_2 and L_3; (b) Discretization of grains A, B and C into 'ALAMEL' domains $a, \ldots, f$; (c) Discretization of a grain containing an annealing twin into a stack of domains.

The 'lamel' (Van Houtte et al., 1999) and 'ALAMEL' models (Van Houtte et al., 2005), form the starting points of the present work. In the 'lamel' model (Van Houtte et al., 1999), the polycrystal is regarded as a collection of bicrystals. Each bicrystal is formed by pairing interacting neighboring grains in the microstructure. Individual grains are assumed to deform homogeneously. In the 'ALAMEL' model, grains do not deform homogeneously. Grains are divided into domains, with one domain abutting each grain boundary facet. Conversely, each grain-boundary facet is associated with two domains meeting

at that facet. It is the domains that are taken to deform homogeneously in the 'ALAMEL' model. The polycrystal is regarded as a collection of bicrystals formed by pairs of domains meeting at a grain-boundary facet. Thus, whereas in the 'lamel' model, homogeneity of grain deformation is accorded greater importance, in the 'ALAMEL' model, coupling between domains across a grain boundary is taken to dominate the coupling between multiple domains within the same grain.

The distinctions between the two models are illustrated in connection with the experimental microstructure of Manonukul and Dunne (2004) shown in Fig. 1. The explanation to follow centers around grains A, B and C marked in Fig. 1a. Fig. 1b shows an enlarged view of these grains and also shows their division into 'ALAMEL' domains, $a \ldots, f$. Here, thick and thin lines denote grain boundary facets and domain boundaries, respectively. Deformations of grains A and B are coupled in the 'lamel' model, whereas, in the 'ALAMEL' model, it is the deformation of domain b in grain A and domain c in grain B that are coupled with each other. On the other hand, the deformation of domain d of grain B is coupled to that of domain e of grain C. Deformation of domain d is unaffected by the deformation of any domain in grain A in the 'ALAMEL' model.

Van Houtte et al. (2004, 2005) and Van Houtte et al. (2006) have reported excellent agreement of the texture predicted by the 'ALAMEL' model with that predicted by the full-field crystal plasticity finite element method provided the division of grains into domains is judiciously done. However, no validation of the mechanical anisotropy predictions of the 'ALAMEL' model is presently available.

The 'ALAMEL' model, while being superior to both the Taylor and 'lamel' models, also has some deficiencies. First, each 'ALAMEL' pair of domains is constrained to undergo the macroscopically imposed deformation. Thus, although 'ALAMEL' domains are less constrained than Taylor or 'lamel' grains, they are over-constrained compared to those in the self-consistent model (Lebensohn and Tomé, 1993), grain interaction model (Engler et al., 2005), or the binary tree based model (Mahesh, 2010). Kanjarla et al. (2010) have recently noted significant deviation from the constraint assumed on 'ALAMEL' pairs from crystal plasticity finite element simulations of an ensemble of four grains. Second, the 'ALAMEL' model completely disregards intra-grain interactions. Such interactions assume added significance in the presence of sub-structural features such as deformation twins, annealing twins (Proust et al., 2007, Bystrzycki et al., 1997), deformation bands or shear bands (Barrett and Levenson, 1940, Liu and Hansen, 1998, Paul et al., 2009). The slip activity within such banded grains is determined by the intra-grain interaction of the banded region with the matrix. Third, the 'ALAMEL' model assumes that pairwise interaction between neighboring domains in the microstructure dominates other, possibly longer range interactions, such as that between a domain and another of its nearest neighbors or one of its next nearest neighbors. Consequences of disregarding these other interactions are not presently quantified.

These shortcomings can be overcome in a straightforward manner by extending the 'ALAMEL' model to account for stacks of an arbitrary number N of codeforming domains. The interface between any two neighboring domains in the stack is assumed planar and oriented identically throughout the stack. Van Houtte et al. (2005) have given an algorithm to discretize grains in a micrograph into domains and 'ALAMEL' units. A systematic procedure to

form stacks of domains involves sequentially gluing neighboring 'ALAMEL' units together. Two neighboring 'ALAMEL' units can be glued together provided (i) one of the domains of each of the 'ALAMEL' units belong to the same grain and (ii) the grain boundaries contained in the two 'ALAMEL' units have similar orientations (i.e., their relative inclinations fall within a prescribed threshold). This procedure will result in the deterministic sub-division of the original micrograph into 'stacks' of different sizes such that every material point in the micrograph will appear in one of the stacks. Statistical correpondence between the original micrograph and the stack representation is therefore automatic, not only for texture but also for the orientation of the grain boundary facets.

The three largest 'stacks' (by area) obtained according to the foregoing conditions from the micrograph are shown in Fig. 1a. Intra-grain boundaries are absent in this micrograph. Fig. 1c schematically illustrates the sub-division of a grain in the presence of an intra-granular boundary such as an annealing twin. The twin is represented as domain c, while the matrix regions surrounding the twin are represented by domains b and d. These domains may also be connected with domains of their neighboring grains, such as a and e to form a stack. The 'stack' model can thus both reduce the constraint on individual domains and account for intra-granular boundaries.

The 'stack' model of a polycrystal resembles the binary tree based model (Mahesh, 2009, 2010) in that interaction between neighboring domains is the central consideration of both models. In this respect, they differ from the self-consistent models (Molinari et al., 1987, Lebensohn and Tomé, 1993) where the key interaction considered is that between a grain and the homogeneous effective medium representing the entire polycrystal. However, whereas the

'stack' model accounts for serial interaction between many domains, the binary tree based model treats interactions between pairs of domain sub-aggregates. The 'stack' model is thus a better physical representation for microstructures wherein banding within grains, as shown in Fig. 1c, is prominent.

In the present work, we develop the 'stack' model of a polycrystal. In Sec. 2 we develop the flow law and consistency conditions for the general 'stack' model and in Sec. 3 we provide an efficient algorithm for its solution in the case of an idealized two dimensional polycrystal. Sec. 4 returns to the aforementioned questions regarding interactions between multiple domains and its effect on the predicted macroscopic response.

2 The 'stack' model

After recapitulating the standard rate-independent crystal plasticity framework (Havner, 1992, Kocks et al., 1998, Asaro and Lubarda, 2006) in Sec. 2.1 below, we develop continuity condition, flow law and consistency equations for the present 'stack' model in Sec. 2.2.

2.1 Plastic deformation of a domain

2.1.1 Standard rate-independent crystal plasticity

Throughout, we assume that domains deform homogeneously following a rigid-plastic rate-independent volume preserving constitutive law. Denoting the

strain-rate of domain g by $\dot{\boldsymbol{\epsilon}}^{[g]}$, we take

$$\dot{\boldsymbol{\epsilon}}^{[g]} = \sum_{s=1}^{S} \dot{\gamma}_s^{[g]} \boldsymbol{m}_s^{[g]}, \tag{1}$$

following the Taylor-Bishop-Hill formulation (Taylor, 1938, Bishop and Hill, 1951). $\dot{\gamma}_s^{[g]}$ in Eq. (1) denotes the slip-rate of slip system $s \in \{1, 2, \ldots, S\}$ and $\boldsymbol{m}_s^{[g]}$ denotes the Schmid tensor of slip system s

$$\boldsymbol{m}_s^{[g]} = (\boldsymbol{b}_s^{[g]} \otimes \boldsymbol{n}_s^{[g]} + \boldsymbol{n}_s^{[g]} \otimes \boldsymbol{b}_s^{[g]})/2, \tag{2}$$

where $\boldsymbol{b}_s^{[g]}$ is the Burger's vector or unit slip directional vector of slip system s with slip plane normal $\boldsymbol{n}_s^{[g]}$.

Let $\boldsymbol{T}^{[g]}$ be the Cauchy stress in domain g and let its deviatoric part be $\boldsymbol{\sigma}^{[g]}$. Thus,

$$\boldsymbol{\sigma}^{[g]} = \boldsymbol{T}^{[g]} - p^{[g]} \boldsymbol{I}, \tag{3}$$

where, $p^{[g]} = \mathrm{tr}(\boldsymbol{T}^{[g]})/3$ is the hydrostatic pressure in domain g.

Anticipating that standard linear programming will be used to solve the crystal plasticity model, we take $\dot{\gamma}_s^{[g]} \geq 0$, for all s. Schmid's law (Kocks et al., 1998) states that slip system s may have non-zero slip-rate only if the resolved shear stress, $\boldsymbol{\sigma}^{[g]} : \boldsymbol{m}_s^{[g]} \equiv \mathrm{tr}(\boldsymbol{\sigma}^{[g]} {\boldsymbol{m}_s^{[g]}}^T)$, equals the critical resolved shear stress on slip system s, $\tau_s^{[g]}$. Thus,

$$\dot{\gamma}_s^{[g]} \begin{cases} \geq 0, & \text{if } \boldsymbol{\sigma}^{[g]} : \boldsymbol{m}_s^{[g]} = \tau_s^{[g]}, \\ = 0, & \text{if } \boldsymbol{\sigma}^{[g]} : \boldsymbol{m}_s^{[g]} < \tau_s^{[g]}. \end{cases} \tag{4}$$

Condition (4) implies that the yield surface of the rate-independent single crystal is made of S smooth surfaces $f_s^{[g]}$ given by

$$f_s^{[g]} = \tau_s^{[g]} - \boldsymbol{\sigma}^{[g]} : \boldsymbol{m}_s^{[g]} = 0, \quad s \in \{1, 2, ..S\}. \tag{5}$$

$f_s^{[g]}$ is independent of $p^{[g]}$, i.e., the plastic response of the single crystal is assumed to be pressure-insensitive. Slip system s^* is said to be critical if $f_{s^*}^{[g]} = 0$. Clearly, according to Eq. (4), non-critical slip systems must necessarily have zero slip-rates.

Chin and Mammel (1969) have shown that Taylor's principle (Taylor, 1938), which asserts that for given $\dot{\boldsymbol{\epsilon}}^{[g]}$ of all possible slip-rate combinations $\{\dot{\gamma}_s^{[g]}, s \in \{1, \ldots, S\}\}$ that respect the constraint given by Eq. (1), those which minimize the plastic power of deformation

$$\dot{W}_p^{[g]} = \sum_{s=1}^{S} \tau_s^{[g]} \dot{\gamma}_s^{[g]} \tag{6}$$

automatically satisfy Eq. (4). For the optimal set of slip-rates, Chin and Mammel (1969) further established the equivalence of the Taylor (Taylor, 1938) and Bishop-Hill (Bishop and Hill, 1951) formulations and established the equivalence of the internal and external plastic powers, i.e., $\sum_s \tau_s^{[g]} \dot{\gamma}_s^{[g]} = \boldsymbol{\sigma}^{[g]} : \dot{\boldsymbol{\epsilon}}^{[g]}$. Van Houtte and Aernoudt (1975a,b) have given a computational procedure for the analysis of a polycrystal model by reducing Eqs. (6) and (1) to the form of a standard linear program.

2.1.2 Kinematics

The deformation gradient $\boldsymbol{F}^{[g]}$ of a rigid-plastic domain can be decomposed (Lee, 1969) as $\boldsymbol{F}^{[g]} = \boldsymbol{R}_{\text{lat}}^{[g]} \boldsymbol{F}_p^{[g]}$, where $\boldsymbol{R}_{\text{lat}}^{[g]}$ denotes an orthonormal tensor signifying lattice rotation, and $\boldsymbol{F}_p^{[g]}$ is the part of the deformation gradient accommodated through slip-rate. The evolution of the deformation gradient is given by

(e.g., Gurtin (1981))

$$\dot{\boldsymbol{F}}^{[g]} = \boldsymbol{L}^{[g]}\boldsymbol{F}^{[g]}, \tag{7}$$

where $\boldsymbol{L}^{[g]}$ denotes the velocity gradient of the domain. Rice (1971) related the evolution of $\boldsymbol{F}_p^{[g]}$ to slip-rate through the flow rule

$$\dot{\boldsymbol{F}}_p^{[g]} = \boldsymbol{L}_p^{[g]}\boldsymbol{F}_p^{[g]}, \tag{8}$$

where,

$$\boldsymbol{L}_p^{[g]} = \sum_{s=1}^{S} \dot{\gamma}_s^{[g]} ({\boldsymbol{R}_{\text{lat}}^{[g]}}^T \boldsymbol{b}_s^{[g]}) \otimes ({\boldsymbol{R}_{\text{lat}}^{[g]}}^T \boldsymbol{n}_s^{[g]}) = {\boldsymbol{R}_{\text{lat}}^{[g]}}^T \left[\sum_{s=1}^{S} \dot{\gamma}_s^{[g]} \boldsymbol{b}_s^{[g]} \otimes \boldsymbol{n}_s^{[g]} \right] \boldsymbol{R}_{\text{lat}}^{[g]}. \tag{9}$$

${\boldsymbol{R}_{\text{lat}}^{[g]}}^T \boldsymbol{b}_s^{[g]}$ and ${\boldsymbol{R}_{\text{lat}}^{[g]}}^T \boldsymbol{n}_s$ are the slip direction, and slip plane normal, respectively, of the s-th slip system in the reference configuration corresponding to $\boldsymbol{F}^{[g]} = \boldsymbol{F}_p^{[g]} = \boldsymbol{I}$. The term within square brackets in the last step of Eq. (9) is based on the orientation of the slip systems in the current (lattice rotated) configuration, and will occur more frequently in what follows. It is called the slip-rate tensor (Fleck et al., 2003), and is denoted

$$\boldsymbol{L}_{\text{ss}}^{[g]} = \sum_{s=1}^{S} \dot{\gamma}_s^{[g]} \boldsymbol{b}_s^{[g]} \otimes \boldsymbol{n}_s^{[g]}. \tag{10}$$

It is clear that $\boldsymbol{L}_p^{[g]} = {\boldsymbol{R}_{\text{lat}}^{[g]}}^T \boldsymbol{L}_{\text{ss}}^{[g]} \boldsymbol{R}_{\text{lat}}^{[g]}$. The symmetric part of the slip rate tensor, $\boldsymbol{L}_{\text{ss}}^{[g]}$, is the strain-rate of the domain, $\dot{\boldsymbol{\epsilon}}^{[g]} = (\boldsymbol{L}_{\text{ss}}^{[g]} + {\boldsymbol{L}_{\text{ss}}^{[g]}}^T)/2$, given by Eq. (1).

The lattice rotation tensor $\boldsymbol{R}_{\text{lat}}^{[g]}$ of a domain evolves as

$$\dot{\boldsymbol{R}}_{\text{lat}}^{[g]} = \boldsymbol{\Omega}_{\text{lat}}^{[g]} \boldsymbol{R}_{\text{lat}}^{[g]}, \tag{11}$$

where, $\boldsymbol{\Omega}_{\text{lat}}^{[g]}$ is skew-symmetric and is called the lattice spin tensor. The velocity gradient of the domain is comprised of contributions from slip rate, and lattice spin as

$$\boldsymbol{L}^{[g]} = \boldsymbol{L}_{\text{ss}}^{[g]} + \boldsymbol{\Omega}_{\text{lat}}^{[g]}. \tag{12}$$

Taken together with Eqs. (8), (9), (10) and (11), Eq. (12) implies (Pierce et al., 1983)

$$\boldsymbol{L}^{[g]} = \dot{\boldsymbol{F}}^{[g]}\boldsymbol{F}^{[g]^{-1}} = \boldsymbol{R}^{[g]}_{\text{lat}}\dot{\boldsymbol{F}}^{[g]}_{p}\boldsymbol{F}^{[g]^{-1}}_{p}\boldsymbol{R}^{[g]^{T}}_{\text{lat}} + \dot{\boldsymbol{R}}^{[g]}_{\text{lat}}\boldsymbol{R}^{[g]^{T}}_{\text{lat}}. \tag{13}$$

2.1.3 Hardening

Sub-structural processes that accompany accumulating slip-rate typically affect the state of the domain (Cuitiño and Ortiz, 1992). The state evolution is represented as the evolution of the critical resolved shear stress ($\tau_s^{[g]}$) following the standard form (Hill, 1966, Kocks et al., 1998)

$$\dot{\tau}_s^{[g]} = \frac{d\tau^{[g]}}{d\Gamma^{[g]}} \sum_{s'=1}^{S} H_{ss'}\dot{\gamma}_{s'}^{[g]}, \tag{14}$$

where $[H]$ is the latent hardening matrix and $\Gamma^{[g]} = \sum_{s=1}^{S} \gamma_s^{[g]}$, is the total accumulated slip in domain g. In the present work, for simplicity, we take $\tau^{[g]}$ to have a power law dependence on $\Gamma^{[g]}$, i.e.,

$$\tau^{[g]}(\Gamma^{[g]}) = \tau_0 + \theta_1(\Gamma_0 + \Gamma^{[g]})^p, \tag{15}$$

where p is called the hardening index, τ_0, a scalar parameter, denotes the initial critical resolved shear stress and θ_1 is the hardening rate.

2.2 Plastic deformation of a 'stack'

2.2.1 Geometry and notation

A stack of N domains, the central object of study in the present work, is shown in Fig. 2a. Parallelepiped-shaped domains, $g \in \{1, 2, \ldots, N\}$, equal in all dimensions, except possibly the thickness $t^{[g]}$, are stacked as shown in

Fig. 2a. The volume of fraction, $\rho^{[g]}$, of domain g is then

$$\rho^{[g]} = \frac{t^{[g]}}{\sum_{l=1}^{N} t^{[l]}}. \tag{16}$$

We assume that the stacking is repeated periodically *ad infinitum* so that neighbors of domain g in the stack are $g+1 \mod N$ and $g-1 \mod N$. In particular, the two neighbors of domain 1 in the stack are domain N and domain 2 and those of domain N are domain $N-1$ and domain 1. In the case that $N = 2$ the geometry of the 'stack' model reduces to that of the twinning models of Lebensohn et al. (1998a), Lebensohn (1999) and the 'lamel' or 'ALAMEL' models of Van Houtte et al. (1999, 2002, 2005).

Domain boundaries between adjacent domains are taken to be planar and identically orientated with the normal vector $\boldsymbol{\nu}$, as shown in Fig. 2a. Two sets of cartesian coordinates: the sample coordinate system xyz and a domain boundary coordinate system XYZ with its Y-axis always aligned with the normal vector $\boldsymbol{\nu}$ are also defined.

Since domains g and domain boundaries i play an important role in the following considerations, we adopt the following conventions. Quantities associated with domains are indicated by superscripts surrounded by square brackets, e.g., $t^{[g]}$ for the thickness of domain g in Eq. (16), while quantities associated with interfaces are indicated by superscripts surrounded by parantheses, e.g., $\boldsymbol{\lambda}^{(i)}$ denoting the Hadamard characteristic segment of domain boundary i in Eq. (28) below. Secondly, domains above and below, the domain boundary i will be denoted as $[a(i)]$ and $[b(i)]$, respectively, while the domain-boundaries surrounding interface i will be called $(a(i))$ and $(b(i))$, respectively, as shown in Fig. 2b. Note that use of the terms 'above' and 'below' are for mnemonical purposes only; their consistent interchange will not affect any other aspect of

the present model.

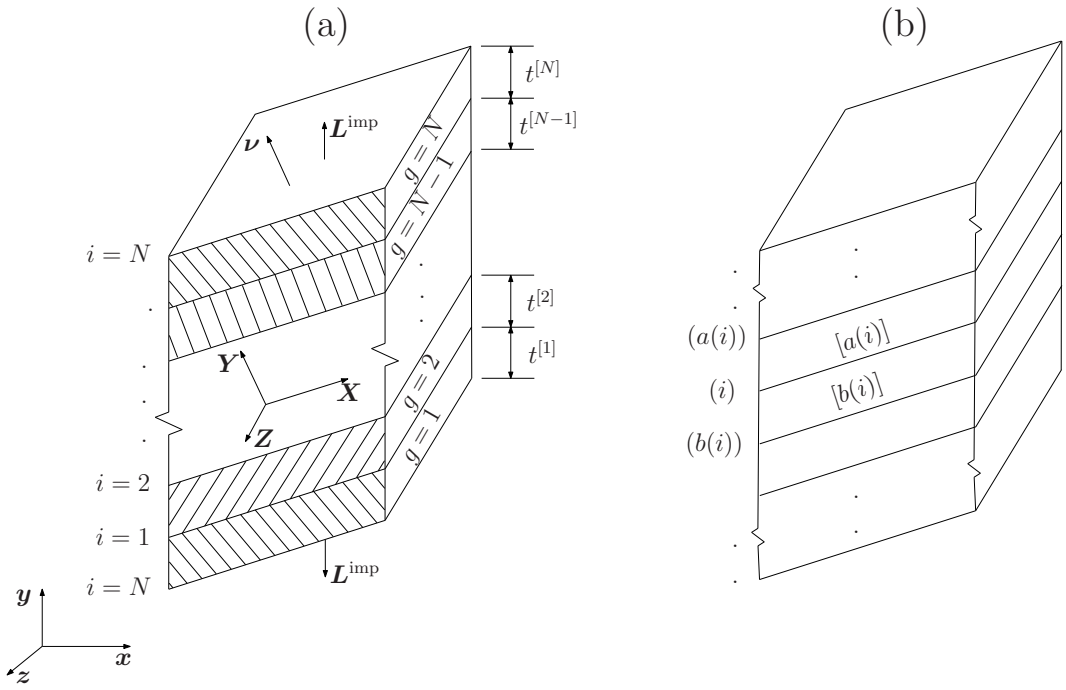

Fig. 2. (a) The 'stack' model comprised of N domains. (b) Nomenclature for domain and domain boundaries.

2.2.2 Kinematics of 'stack'

We may now extend the kinematic notions defined for a domain in Sec. 2.1.2 to a 'stack'. The velocity gradient of a 'stack' is taken as the volume fraction weighted average of that of its constituent domains, i.e.,

$$\bar{\boldsymbol{L}} = \sum_{g=1}^{N} \rho^{[g]} \boldsymbol{L}^{[g]}. \tag{17}$$

If $\bar{\boldsymbol{F}}$ denotes the deformation gradient of the 'stack', in analogy with Eq. (7) for single domains, we define

$$\dot{\bar{\boldsymbol{F}}} = \bar{\boldsymbol{L}}\bar{\boldsymbol{F}}. \tag{18}$$

The domain boundary normal $\boldsymbol{\nu}$, defined in Sec. 2.2.1 is assumed to evolve

with the shape of the 'stack', as given by $\bar{\boldsymbol{F}}$. Thus, if $\boldsymbol{\nu}_0$ is the normal vector when $\bar{\boldsymbol{F}} = \boldsymbol{I}$, according to Nanson's formula (Gurtin, 1981),

$$\boldsymbol{\nu} = \frac{\bar{\boldsymbol{F}}^{-T}\boldsymbol{\nu}_0}{\|\bar{\boldsymbol{F}}^{-T}\boldsymbol{\nu}_0\|}. \tag{19}$$

Time differentiating Eq. (19) and simplification using Eq. (18) gives

$$\dot{\boldsymbol{\nu}} = (\boldsymbol{\nu} \otimes \bar{\boldsymbol{L}}^T\boldsymbol{\nu} - \bar{\boldsymbol{L}}^T)\boldsymbol{\nu}. \tag{20}$$

2.2.3 Constraints

In the present work, we assume the full constraints boundary conditions,

$$\bar{\boldsymbol{L}} = \boldsymbol{L}^{\text{imp}}, \tag{21}$$

where $\bar{\boldsymbol{L}}$ is defined by Eq. (17). The present formulation can, however, easily be extended to accommodate other constraints, such as relaxed constraint, self-consistent constraint, etc as discussed by Mahesh (2009).

Eq. (21) subsumes the imposed strain-rate constraint, viz.,

$$\bar{\dot{\boldsymbol{\epsilon}}} = \sum_{g=1}^{N} \rho^{[g]}\dot{\boldsymbol{\epsilon}}^{[g]} = \dot{\boldsymbol{\epsilon}}^{\text{imp}} = (\boldsymbol{L}^{\text{imp}} + \boldsymbol{L}^{\text{imp}^T})/2. \tag{22}$$

2.2.4 Continuity and boundary conditions

Continuity conditions in a 'stack of slabs' are straightforward extensions of the notions in the two-domain models of Lebensohn et al. (1998a), Lebensohn (1999) and Van Houtte et al. (1999, 2002, 2005); they are summarily described here following the framework and notation of Mahesh (2009, 2010).

Traction continuity across domain boundary i requires that

$$(\boldsymbol{T}^{[a(i)]} - \boldsymbol{T}^{[b(i)]})\boldsymbol{\nu} = \boldsymbol{0}, \tag{23}$$

where $\boldsymbol{T}^{[a(i)]}$ and $\boldsymbol{T}^{[b(i)]}$ are the Cauchy stresses in the domains meeting at domain boundary i. In terms of the decomposition of the Cauchy stress into deviatoric and pressure components, given by Eq. (3), Eq. (23) implies

$$[(\boldsymbol{\sigma}^{[a(i)]} - \boldsymbol{\sigma}^{[b(i)]}) + (p^{[a(i)]} - p^{[b(i)]})\boldsymbol{I}]\boldsymbol{\nu} = \boldsymbol{0}. \tag{24}$$

As noted in Sec. 2.1, the plastic response of the domains $a(i)$ and $b(i)$ are insensitive to the pressures $p^{[a(i)]}$ and $p^{[b(i)]}$. These pressures may therefore, presently be selected arbitrarily. The vector equation given by Eq. (23) implies three scalar equations one of which is given as

$$(\boldsymbol{T}^{[a(i)]} - \boldsymbol{T}^{[b(i)]})\boldsymbol{\nu} \cdot \boldsymbol{\nu} = 0. \tag{25}$$

This equation can be identically satisfied by selecting

$$p^{[a(i)]} - p^{[b(i)]} = -(\boldsymbol{\sigma}^{[a(i)]} - \boldsymbol{\sigma}^{[b(i)]})\boldsymbol{\nu} \cdot \boldsymbol{\nu}. \tag{26}$$

Assuming Eq. (26), Eq. (24) becomes

$$\left\{(\boldsymbol{\sigma}^{[a(i)]} - \boldsymbol{\sigma}^{[b(i)]}) - \boldsymbol{\nu} \otimes (\boldsymbol{\sigma}^{[a(i)]} - \boldsymbol{\sigma}^{[b(i)]})\boldsymbol{\nu}\right\}\boldsymbol{\nu} = \boldsymbol{0}. \tag{27}$$

The vector equation, Eq. (27) gives the condition for traction continuity in terms of deviatoric stresses. One of the three scalar equations contained therein, viz., $\left\{(\boldsymbol{\sigma}^{[a(i)]} - \boldsymbol{\sigma}^{[b(i)]}) - \boldsymbol{\nu} \otimes (\boldsymbol{\sigma}^{[a(i)]} - \boldsymbol{\sigma}^{[b(i)]})\boldsymbol{\nu}\right\}\boldsymbol{\nu} \cdot \boldsymbol{\nu} = 0$, is identically satisfied; Eq. (27) therefore amounts only to demanding continuity of the shear components of the deviatoric stresses across the interface between $[a(i)]$ and $[b(i)]$. Traction continuity required by Eq. (27) is applicable to both $\mathscr{E}$-type and $\mathscr{S}$-type continuity conditions.

As noted in Sec. 1, $\mathscr{E}$-type continuity conditions between neighboring domains requires velocity continuity across domain boundary i. In this case, following

Hill (1961), we have

$$[\![\boldsymbol{L}^{(i)}]\!] = \boldsymbol{L}^{[a(i)]} - \boldsymbol{L}^{[b(i)]} = \boldsymbol{\lambda}^{(i)} \otimes \boldsymbol{\nu}, \tag{28}$$

for some vector $\boldsymbol{\lambda}^{(i)}$, called Hadamard's characteristic segment of interface i. The symmetric part of Eq. (28) demands strain-rate compatibility across domain boundary i, viz.,

$$[\![\dot{\boldsymbol{\epsilon}}^{(i)}]\!] = \dot{\boldsymbol{\epsilon}}^{[a(i)]} - \dot{\boldsymbol{\epsilon}}^{[b(i)]} = \left(\boldsymbol{\lambda}^{(i)} \otimes \boldsymbol{\nu} + (\boldsymbol{\lambda}^{(i)} \otimes \boldsymbol{\nu})^T\right)/2, \tag{29}$$

where,

$$\boldsymbol{\lambda}^{(i)} = 2[\![\dot{\boldsymbol{\epsilon}}^{(i)}]\!]\boldsymbol{\nu} + ([\![\dot{\boldsymbol{\epsilon}}^{(i)}]\!]\boldsymbol{\nu} \cdot \boldsymbol{\nu})\boldsymbol{\nu}, \tag{30}$$

as shown by Mahesh (2006). To obtain the lattice spins in domains $[a(i)]$ and $[b(i)]$, $\boldsymbol{\Omega}^{[a(i)]}$ and $\boldsymbol{\Omega}^{[b(i)]}$, respectively, we rewrite Eq. (28) using Eq. (12) as

$$\boldsymbol{L}_{ss}^{[a(i)]} + \boldsymbol{\Omega}^{[a(i)]} - (\boldsymbol{L}_{ss}^{[b(i)]} + \boldsymbol{\Omega}^{[b(i)]}) = \boldsymbol{\lambda}^{(i)} \otimes \boldsymbol{\nu}. \tag{31}$$

Summing both sides of Eq. (31) over all domain-boundaries i results in telescopic cancelation of the left side so that $\sum_{i=1}^{N} \boldsymbol{\lambda}^{(i)} \otimes \boldsymbol{\nu} = \boldsymbol{0}$ for all $\boldsymbol{\nu}$. Thus,

$$\sum_{i=1}^{N} \boldsymbol{\lambda}^{(i)} = \boldsymbol{0}. \tag{32}$$

Similarly, expressing the boundary condition, Eq. (21), in terms of its decomposition into slip-rate and spin tensors following Eq. (12) gives

$$\sum_{g=1}^{N} \rho^{[g]} \left(\boldsymbol{L}_{ss}^{[g]} + \boldsymbol{\Omega}^{[g]}\right) = \boldsymbol{L}^{\text{imp}}. \tag{33}$$

After eliminating all but one of the terms $\boldsymbol{L}_{ss}^{[g]} + \boldsymbol{\Omega}^{[g]}$ from Eqs. (31) and (33), we obtain

$$\boldsymbol{L}_{ss}^{[g]} + \boldsymbol{\Omega}^{[g]} = \boldsymbol{L}^{\text{imp}} - \sum_{k=1}^{N} \rho^{[(g+k) \bmod N]} \sum_{m=0}^{k-1} \boldsymbol{\lambda}^{((g+m) \bmod N)} \otimes \boldsymbol{\nu}, \tag{34}$$

which, upon further algebraic manipulation using Eq. (32) gives

$$\boldsymbol{\Omega}^{[g]} = \boldsymbol{L}^{\text{imp}} - \boldsymbol{L}^{[g]}_{ss} + \sum_{k=1}^{N} \left[\sum_{l=1}^{k} \rho^{[(g+l) \bmod N]} \right] \boldsymbol{\lambda}^{((g+k) \bmod N)} \otimes \boldsymbol{\nu}. \tag{35}$$

Substituting the expression for $\boldsymbol{\lambda}^{(i)}$ from Eq. (30) into Eq. (35) gives

$$\boldsymbol{\Omega}^{[g]} = \text{skew} \left(\boldsymbol{L}^{\text{imp}} - \boldsymbol{L}^{[g]}_{ss} + \boldsymbol{\Phi}^{[g]} - \boldsymbol{\Phi}^{\text{imp}} \right), \tag{36}$$

where,

$$\begin{aligned} \boldsymbol{\Phi}^{[g]} &= \left[2\dot{\boldsymbol{\epsilon}}^{[g]}\boldsymbol{\nu} - (\dot{\boldsymbol{\epsilon}}^{[g]}\boldsymbol{\nu} \cdot \boldsymbol{\nu})\boldsymbol{\nu} \right] \otimes \boldsymbol{\nu} \text{ and} \\ \boldsymbol{\Phi}^{\text{imp}} &= \left[2\dot{\boldsymbol{\epsilon}}^{\text{imp}}\boldsymbol{\nu} - (\dot{\boldsymbol{\epsilon}}^{\text{imp}}\boldsymbol{\nu} \cdot \boldsymbol{\nu})\boldsymbol{\nu} \right] \otimes \boldsymbol{\nu}. \end{aligned} \tag{37}$$

Expressed in terms of slip-rates using Eqs. (10) and (1), Eq. (36) becomes

$$\boldsymbol{\Omega}^{[g]} = \text{skew} \left[\boldsymbol{L}^{\text{imp}} - \boldsymbol{\Phi}^{\text{imp}} - \sum_{s=1}^{S} \dot{\gamma}^{[g]}_{s} \boldsymbol{\psi}^{[g]}_{s} \right], \tag{38}$$

where,

$$\boldsymbol{\psi}^{[g]}_{s} = \boldsymbol{b}^{[g]}_{s} \otimes \boldsymbol{n}^{[g]}_{s} - \left[2\boldsymbol{m}^{[g]}_{s}\boldsymbol{\nu} - (\boldsymbol{m}^{[g]}_{s}\boldsymbol{\nu} \cdot \boldsymbol{\nu})\boldsymbol{\nu} \right] \otimes \boldsymbol{\nu}$$

The foregoing equations may be classified into two groups: (i) Eqs. (1), (21), (27), (29), subject to conditions given by Eq. (4), which describe domain deformation through slip-rate in the 'stack' model, and (ii) Eqs. (36) and (38) which give the lattice spin that must accompany the deformation to ensure compatibility between domains. The unknowns in the first group of equations are the slip-rates, $\dot{\gamma}^{[g]}_{s}$, for all slip systems $s \in \{1, 2, \ldots, S\}$ in each domain $g \in \{1, 2, \ldots N\}$. Each of the two groups of equations is closed.

It is well-known that the solution of equations of group (i) above for a single crystal may be non-unique (Havner, 1992). The multiplicity of solutions increases N-fold in the case of the 'stack' model as the following simple example shows. Suppose that a single crystal accommodates the strain-rate

$\boldsymbol{\epsilon}^{\text{imp}}$, imposed upon it by a particular combination of slip-rates, $\{\dot{\gamma}_s^{[0]} : s \in \{1, 2, \ldots, S\}\}$. Let this solution be unique. Regarding the same single crystal as a stack of N identical domains, of volume fractions, $\{\rho^{[g]} : \sum_{g=1}^{N} \rho^{[g]} = 1\}$, we find that the equations of group (i) are satisfied if $\dot{\gamma}_s^{[g]} = \beta^{[g]}\dot{\gamma}_s^{[0]}$ for any choice of $\beta^{[g]}$, $g \in \{1, 2, \ldots, N\}$, subject only to the constraints that $\beta^{[g]} \geq 0$ and $\sum_{g=1}^{N} \beta^{[g]}\rho^{[g]} = 1$. Thus, even if solution $\{\dot{\gamma}_s^{[0]}\}$ of the deformation problem of a single crystal were unique, the corresponding 'stack' model may admit multiple solutions.

2.2.5 Consistency condition

Non-uniqueness of the solution of the deformation problem is a source of instability in the solution algorithm (Anand and Kothari, 1996). To avoid non-uniqueness of slip-rates in single crystals, Renouard and Wintenberger (1981) proposed the minimum second order plastic work postulate, according to which the slip-rates which correspond to the minimum second-order plastic work will be preferred. Their postulate has also been systematically described by Havner and Chidambarrao (1987). In a series of works (Le and Havner, 1985, Fuh and Havner, 1986, Havner and Chidambarrao, 1987) summarized by Havner (1992), another postulate, called the consistency condition has been proposed. The consistency condition reduces, but may not eliminate the degree of non-uniqueness of the slip-rate solution in the case of single crystals. Havner and Chidambarrao (1987) and Havner (1992) have shown that of the two postulates, the consistency condition is more successful in predicting the experimentally observed pattern of slip-activity in single crystals of f.c.c. materials. Here, we extend the consistency conditions to the present 'stack' model.

The consistency condition requires that the stress in each domain evolve with the yield surface of that domain (Havner, 1992). In terms of the yield function, $f_s^{[g]}$ defined in Eq. (5), this implies that for all critical slip systems s in domain g,

$$\dot{f}_s^{[g]} = \dot{\overline{\tau_s^{[g]} - \boldsymbol{\sigma}^{[g]} : \boldsymbol{m}_s^{[g]}}} = 0, \quad \text{if } f_s^{[g]} = 0. \tag{39}$$

Thus,

$$(\dot{\boldsymbol{\sigma}}^{[g]} \colon \boldsymbol{m}_s^{[g]} + \boldsymbol{\sigma}^{[g]} \colon \dot{\boldsymbol{m}}_s^{[g]}) = \dot{\tau}_s^{[g]}, \quad \text{if } f_s^{[g]} = 0. \tag{40}$$

Time differentiating Eq. (2), and substituting $\dot{\boldsymbol{b}}_s^{[g]} = \boldsymbol{\Omega}^{[g]} \boldsymbol{b}_s{}^{[g]}$ and $\dot{\boldsymbol{n}}_s^{[g]} = \boldsymbol{\Omega}^{[g]} \boldsymbol{n}_s{}^{[g]}$ we obtain

$$\begin{aligned} \dot{\boldsymbol{m}}_s^{[g]} &= \operatorname{sym}\left[\boldsymbol{\Omega}^{[g]} \left(\boldsymbol{b}_s^{[g]} \otimes \boldsymbol{n}_s^{[g]}\right) - \left(\boldsymbol{b}_s^{[g]} \otimes \boldsymbol{n}_s^{[g]}\right) \boldsymbol{\Omega}^{[g]}\right] \\ &= 2 \operatorname{sym}\left(\boldsymbol{\Omega}^{[g]} \boldsymbol{m}_s^{[g]}\right). \end{aligned} \tag{41}$$

Substituting Eq. (41) into the left side of Eq. (40), and using Eq. (14) to expand the right side of Eq. (40), we obtain the consistency condition in the form

$$\left(\dot{\boldsymbol{\sigma}}^{[g]} - \boldsymbol{\Omega}^{[g]} \boldsymbol{\sigma}^{[g]} + \boldsymbol{\sigma}^{[g]} \boldsymbol{\Omega}^{[g]}\right) : \boldsymbol{m}_s^{[g]} = \frac{d\tau(\Gamma^{[g]})}{d\Gamma^{[g]}} \sum_{s'=1}^{S} H_{ss'} \dot{\gamma}_{s'}^{[g]}. \tag{42}$$

Substituting for $\boldsymbol{\Omega}^{[g]}$ from Eq. (38) and using Eq. (21), the consistency condition in terms of slip rates is

$$\dot{\boldsymbol{\sigma}}^{[g]} \colon \boldsymbol{m}_s^{[g]} + \sum_{s'=1}^{S} \left[\boldsymbol{\chi}_{s'}^{[g]} \colon \boldsymbol{m}_{s'}^{[g]} - \frac{d\tau(\Gamma^{[g]})}{d\Gamma^{[g]}} H_{ss'}\right] \dot{\gamma}_{s'}^{[g]} = \boldsymbol{\zeta}^{[g]} \colon \boldsymbol{m}_s^{[g]}, \tag{43}$$

where,

$$\begin{aligned} \boldsymbol{\zeta}^{[g]} &= (\boldsymbol{L}^{\text{imp}} - \boldsymbol{\Phi}^{\text{imp}}) \boldsymbol{\sigma}^{[g]} - \boldsymbol{\sigma}^{[g]} (\boldsymbol{L}^{\text{imp}} - \boldsymbol{\Phi}^{\text{imp}}), \\ \boldsymbol{\chi}_s^{[g]} &= \boldsymbol{\psi}_s^{[g]} \boldsymbol{\sigma}^{[g]} - \boldsymbol{\sigma}^{[g]} \boldsymbol{\psi}_s^{[g]}. \end{aligned} \tag{44}$$

Additionally, the stress-rates in neighboring domains in the stack must also be so as to maintain continuity of the traction rate at the domain bound-

aries. Thus, for each domain-boundary i, $\dot{\overline{(\boldsymbol{T}^{[a(i)]} - \boldsymbol{T}^{[b(i)]})\boldsymbol{\nu}}} = \boldsymbol{0}$, or in terms of deviatoric stress from Eq. (27),

$$\dot{\overline{\left\{(\boldsymbol{\sigma}^{[a(i)]} - \boldsymbol{\sigma}^{[b(i)]}) - \boldsymbol{\nu} \otimes (\boldsymbol{\sigma}^{[a(i)]} - \boldsymbol{\sigma}^{[b(i)]})\boldsymbol{\nu}\right\}\boldsymbol{\nu}}} = \boldsymbol{0}. \tag{45}$$

After some algebraic manipulation, the traction rate continuity condition across the interface i is given by

$$\left\{(\dot{\boldsymbol{\sigma}}^{[a(i)]} - \dot{\boldsymbol{\sigma}}^{[b(i)]}) - \boldsymbol{\nu} \otimes (\dot{\boldsymbol{\sigma}}^{[a(i)]} - \dot{\boldsymbol{\sigma}}^{[b(i)]})\boldsymbol{\nu}\right\}\boldsymbol{\nu} = -\boldsymbol{\Psi}_1^{(i)} + \boldsymbol{\Psi}_2^{(i)} + \boldsymbol{\Psi}_3^{(i)}, \tag{46}$$

where,

$$\begin{aligned}
\boldsymbol{\Psi}_1^{(i)} &= \left\{(\boldsymbol{\sigma}^{[a(i)]} - \boldsymbol{\sigma}^{[b(i)]}) - (\boldsymbol{\sigma}^{[a(i)]} - \boldsymbol{\sigma}^{[b(i)]})\boldsymbol{\nu} \cdot \boldsymbol{\nu}\right\}\dot{\boldsymbol{\nu}}, \\
\boldsymbol{\Psi}_2^{(i)} &= \left\{\boldsymbol{\nu} \otimes (\boldsymbol{\sigma}^{[a(i)]} - \boldsymbol{\sigma}^{[b(i)]})\dot{\boldsymbol{\nu}}\right\}\boldsymbol{\nu}, \\
\boldsymbol{\Psi}_3^{(i)} &= \left\{\dot{\boldsymbol{\nu}} \otimes (\boldsymbol{\sigma}^{[a(i)]} - \boldsymbol{\sigma}^{[b(i)]})\boldsymbol{\nu}\right\}\boldsymbol{\nu},
\end{aligned} \tag{47}$$

and where the expression for $\dot{\boldsymbol{\nu}}$ is obtained by combining Eqs. (20) and (21):

$$\dot{\boldsymbol{\nu}} = (\boldsymbol{\nu} \otimes \boldsymbol{L}^{\mathrm{imp}^T}\boldsymbol{\nu} - \boldsymbol{L}^{\mathrm{imp}^T})\boldsymbol{\nu}. \tag{48}$$

3 Solution methodology

As noted in Sec. 2.2.4, Eqs. (1), (21), (27), (29), subject to conditions given by Eq. (4) constitute the governing equations describing domain deformation in the 'stack' model. These equations must be simultaneously satisfied to obtain the slip-rates in the domains comprising the stack: $\{\dot{\gamma}_s^{[g]} : s \in \{1, 2, \ldots, S\}, g \in \{1, 2, \ldots, N\}\}$. In this section, after specifying the crystallography and geometry of an idealized two-dimensional polycrystal (Sec. 3.1), and expressing the governing equations for the problem of deformation in component form (Sec. 3.2), we propose a solution methodology based on linear programming

(Sec. 3.3).

3.1 Geometry and crystallography of a 2D polycrystal

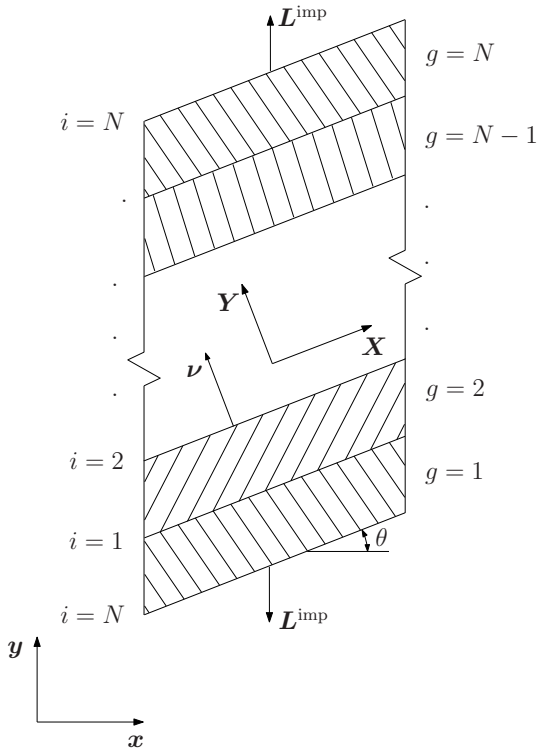

Fig. 3. The two-dimensional 'stack' model comprised of N domains. Coordinate system XY is affixed to the domain boundary.

A two-dimensional 'stack' polycrystal deforming in plane strain in the xy plane, is shown in Fig. 3. All non-zero deviatoric stress components are also assumed to be in-plane. As in the three-dimensional model of Sec. 2.2.1, an XY coordinate system affixed to the domain-boundary is defined, with the Y axis aligned with the normal to the domain-boundary.

Following Asaro (1979, 1983), the crystallography of individual domains in the stack is shown in Fig. 4. Each domain is endowed with two slip systems ($S = 2$) whose shear directions $\boldsymbol{b}_s^{[g]}$ and shear plane normals $\boldsymbol{n}_s^{[g]}$ are confined to

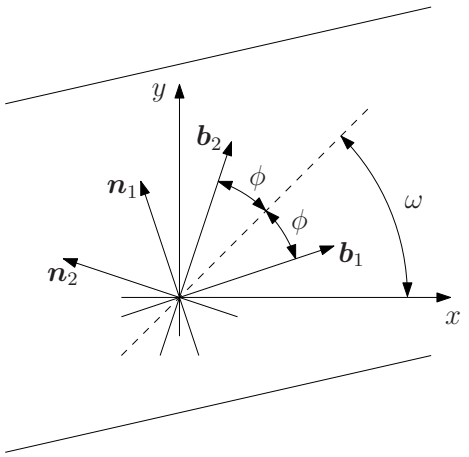

Fig. 4. The slip systems of the two-dimensional domain, following Asaro (1979). $\boldsymbol{b}_s$ and $\boldsymbol{n}_s$ denote the slip direction and slip plane normals of slip systems $s = 1, 2$. ϕ is a characteristic constant of the underlying lattice. ω specifies the lattice orientation.

the xy plane. The angle made by the angle bisector of the acute angle between the slip directions of the two slip systems with the x-axis is denoted ω and is used to describe the lattice orientation of the domain. 2ϕ is the acute angle between the two slip directions. The present hypothetical two-dimensional crystallography can be related to f.c.c. crystals deforming by double slip in tension provided $\pi/6 \leq \phi \leq \pi/5$, and to b.c.c. crystals for $\phi \approx \pi/3$ (Asaro, 1979, 1983). In the present work, we fix $\phi = \pi/6$.

3.2 Boundary and continuity conditions in component form

In the domain boundary fixed XY coordinate system in the two-dimensional 'stack' model, the traction continuity condition, Eq. (27) becomes $\sigma_{12}^{[a(i)]} = \sigma_{12}^{[b(i)]}$ for all domain boundaries i while strain-rate compatibility Eq. (29) becomes $\dot{\epsilon}_{11}^{[a(i)]} = \dot{\epsilon}_{11}^{[b(i)]}$.

Substantial compaction and simplification of notation obtains from using the

Leibfried-Brewer orthonormal basis for symmetric traceless 2×2 matrices (Kocks et al., 1998). The two 2×2 basis matrices are

$$\underline{b}^1 = \frac{1}{\sqrt{2}} \begin{pmatrix} 1 & 0 \\ 0 & -1 \end{pmatrix}, \quad \underline{b}^2 = \frac{1}{\sqrt{2}} \begin{pmatrix} 0 & 1 \\ 1 & 0 \end{pmatrix}. \tag{49}$$

Note that $\underline{b}^\lambda : \underline{b}^\mu = \delta_{\lambda\mu}$. The components of an arbitrary symmetric traceless matrix $\underline{B} = \begin{pmatrix} B_{11} & B_{12} \\ B_{12} & -B_{11} \end{pmatrix}$ in this basis are $B_\lambda = B : \underline{b}^\lambda$, $\lambda = 1, 2$. Thus,

$$(B_1, B_2) = \left(\sqrt{2}B_{11}, \sqrt{2}B_{12}\right). \tag{50}$$

In terms of the Leibfried-Breuwer components, continuity conditions in the XY coordinate frame may be written as

$$\mathscr{E}\text{-type}: \quad \begin{cases} \sigma_2^{[a(i)]} & = \sigma_2^{[b(i)]}, \\ \dot{\epsilon}_1^{[a(i)]} & = \dot{\epsilon}_1^{[b(i)]}. \end{cases} \tag{51}$$

The conditions in Eq. (51) enforce continuity of a shear stress component and a normal strain-rate component across the domain boundary. This represents the component form of $\mathscr{E}$-type continuity described in Secs. 1 and 2.2.4. The latter continuity condition follows from the requirement of compatibility across the domain-boundary. As discussed in Sec. 1 if the latter continuity condition in Eq. (51) is dropped, we obtain the $\mathscr{S}$-type continuity condition:

$$\mathscr{S}\text{-type}: \quad \begin{cases} \sigma_2^{[a(i)]} & = \sigma_2^{[b(i)]}. \end{cases} \tag{52}$$

$\mathscr{E}$-type continuity corresponds to homogeneous deformation of domains wherein compatibility between neighboring domains is preserved without invoking ge-

ometrically necessary dislocations. On the other hand, in $\mathscr{S}$-type continuity geometrically necessary dislocations are assumed to relax incompatibility between the deformation of neighboring domains (Ashby, 1970).

A coordinate transformation will be required to express the continuity conditions of Eq. (51) in the sample xy coordinate system. This is effected by following the procedure adopted by Mahesh (2009, 2010). Let $\underline{R}$ be the orthonormal transformation matrix such that

$$[\boldsymbol{U}]_{XYZ} = \underline{R}^T [\boldsymbol{U}]_{xyz} \underline{R} \tag{53}$$

for any symmetric traceless tensor $\boldsymbol{U}$. Then, in terms of the orthonormal transformation matrix $\underline{\alpha}$ in the Leibfried-Breuwer basis whose components are given by

$$\alpha_{\lambda\mu} = \underline{R}^T \underline{b}^\mu \underline{R} : \underline{b}^\lambda, \tag{54}$$

we have $[U_\lambda]_{XY} = \sum_{\mu=1}^{2} \alpha_{\lambda\mu} [U_\mu]_{xy}$. Using the above transformations, the continuity conditions in Eq. (51) can be written as

$$\begin{aligned} \sum_{\mu=1}^{2} \Xi_\mu \left(\sigma_\mu^{[a(i)]} - \sigma_\mu^{[b(i)]} \right) = 0, \\ \sum_{\mu=1}^{2} \Lambda_\mu \left(\dot{\epsilon}_\mu^{[a(i)]} - \dot{\epsilon}_\mu^{[b(i)]} \right) = 0, \end{aligned} \tag{55}$$

where,

$$\begin{aligned} \underline{\Xi} &= \begin{pmatrix} 0 & 1 \end{pmatrix} \underline{\alpha}, \text{ and} \\ \underline{\Lambda} &= \begin{pmatrix} p & 0 \end{pmatrix} \underline{\alpha}, \end{aligned} \tag{56}$$

where $p = 1$ for $\mathscr{E}$-type domain-boundaries and $p = 0$ for $\mathscr{S}$-type domain-boundaries.

Likewise, the full constraint boundary condition, Eq. (22) can be written in

component form as

$$\bar{\dot{\epsilon}}_\kappa = \dot{\epsilon}_\kappa^{\text{imp}}, \text{for } \kappa \in \{1, 2\}. \tag{57}$$

3.3 Linear programming based solution

Consider the problem of minimizing the plastic power of the 'stack' model

$$\dot{W}_p = \sum_{g=1}^{N} \rho^{[g]} \sum_{s=1}^{S} \tau_s^{[g]} \dot{\gamma}_s^{[g]}, \tag{58}$$

linear in the unknowns, $\dot{\gamma}_s^{[g]}$, subject to the $N + 2$ constraints

$$\begin{aligned} f_\kappa(\underline{\dot{\gamma}}) &= \dot{\epsilon}_\kappa^{\text{imp}} - \sum_{g=1}^{N} \rho^{[g]} \sum_{s=1}^{S} m_{s\kappa}^{[g]} \dot{\gamma}_s^{[g]} = 0, \text{ for } \kappa \in \{1, 2\} \text{ and,} \\ g^{(i)}(\underline{\dot{\gamma}}) &= \sum_{\mu=1}^{2} \Lambda_\mu \sum_{s=1}^{S} \left(m_{s\mu}^{[a(i)]} \dot{\gamma}_s^{[a(i)]} - m_{s\mu}^{[b(i)]} \dot{\gamma}_s^{[b(i)]} \right) = 0, \text{ for } i \in \{1, \ldots, N\}, \end{aligned} \tag{59}$$

also linear in the unknowns, $\dot{\gamma}_s^{[g]}$, where,

$$m_{s\kappa}^{[g]} = \boldsymbol{m}_s^{[g]} : \underline{b}^\kappa, \quad \text{and} \quad m_{s\mu}^{[g]} = \boldsymbol{m}_s^{[g]} : \underline{b}^\mu. \tag{60}$$

The first set of constraints, $f_\kappa(\underline{\dot{\gamma}}) = 0$ in Eq. (59) amounts to the boundary conditions specified in Eq. (57). The second set of constraints $g^{(i)}(\underline{\dot{\gamma}})$ is obtained by substituting Eq. (1) into Eq. (55). Note that in the statement of the optimization problem above, traction continuity is nowhere invoked.

The Lagrangian of the present minimization problem is

$$F(\underline{\dot{\gamma}}, \underline{\vartheta}, \underline{\varphi}) = \dot{W}_p + \sum_{\kappa=1}^{2} \vartheta_\kappa f_\kappa(\underline{\dot{\gamma}}) + \sum_{i=1}^{N} \varphi^{(i)} g^{(i)}(\underline{\dot{\gamma}}), \tag{61}$$

where ϑ_κ and $\varphi^{(i)}$ are the Lagrange multipliers of the constraints $f_\kappa(\underline{\dot{\gamma}})$ and $g^{(i)}(\underline{\dot{\gamma}})$, respectively. The linearity of the objective function and constraints in

$\dot{\gamma}_s^{[g]}$ permits application of the Karush-Kuhn-Tucker optimality conditions

$$\frac{\partial F}{\partial \dot{\gamma}_s^{[g]}} \quad \begin{cases} = 0, & \text{if } \dot{\gamma}_s^{[g]} > 0, \\ \geq 0, & \text{if } \dot{\gamma}_s^{[g]} = 0. \end{cases} \tag{62}$$

Substituting the Lagrangian from Eq. (61) into Eq. (62), and using Eq. (60) we get

$$\tau_s^{[g]} = \left[\sum_{\kappa=1}^{2} \vartheta_\kappa \underline{b}^\kappa + \frac{1}{\rho^{[g]}} \left(\varphi^{(g)} - \varphi^{(b(g))} \right) \sum_{\mu=1}^{2} \Lambda_\mu \underline{b}^\mu \right] : \boldsymbol{m}_s^{[g]}, \tag{63}$$

provided $\dot{\gamma}_s^{[g]} > 0$. Comparison of Eqs. (4) and (63) shows that the deviatoric stress of domain g must be

$$\boldsymbol{\sigma}^{[g]} = \sum_{\kappa=1}^{2} \vartheta_\kappa \underline{b}^\kappa + \frac{1}{\rho^{[g]}} \left(\varphi^{(g)} - \varphi^{(b(g))} \right) \sum_{\mu=1}^{2} \Lambda_\mu \underline{b}^\mu. \tag{64}$$

For $\mathscr{S}$-type domain-boundaries, according to Eq. (56) $\Lambda_\mu = 0$. In this case, the second term in Eq. (64) vanishes, implying that the stress in all the domains of the stack will be uniform.

3.4 Integration over the deformation history

Evolution equations for various variables associated with the 'stack' model of a polycrystal have been derived above: Slip rates are given by the solution of Eqs. (58–59), Eq. (14) describes the evolution of the critical resolved shear stress of systems, Eq. (48) gives the evolution of the inter-domain boundary orientation and Eq. (38) gives the lattice spin rate. These evolutions are integrated over the deformation history using a standard package called `lsode` (Radhakrishnan and Hindmarsh, 1993).

4 Results and discussion

The 'stack' model is now applied to predict the macroscopic mechanical response of idealized two-dimensional polycrystalline aggregate comprising of $n_g = 1024$ domains (after discretizing the grains into domains using the algorithm given in Sec. 1). The initial orientation of the domains, given by ω (Sec. 3.1), is assumed to be uniformly distributed i.e., $\omega \sim U(0, \pi)$. All domains are assumed to have equal volume so that the volume fraction of the g-th domain is $\rho^{[g]} = 1/n_g$. domains are assumed to harden following Eq. (15) with hardening parameters chosen arbitrarily as $\tau_0 = 10$, $\theta_1 = 10$, $\Gamma_0 = 1$ and $p = 1$. Isotropic hardening of the slip systems is assumed, i.e., $H_{ij} = 1$, for $i, j \in \{1, 2\}$.

The polycrystalline aggregate comprised of n_g domains is divided into M 'stacks', each comprised of N domains, so that $MN = n_g$. Fig. 5 shows three possible divisions of an $n_g = 8$ domain aggregate into stacks of size $N = 1$, $N = 2$ and $N = 4$. As noted previously in connection with Eqs. (51) and (52), continuity conditions between neighboring domains in the stack can be of the $\mathscr{E}$-type or $\mathscr{S}$-type. In what follows, we will henceforth refer to the polycrystal model comprised of $M = n_g/N$ stacks of N domains each as the $\mathscr{E}^N$ or $\mathscr{S}^N$ model according as whether $\mathscr{E}$-type or $\mathscr{S}$-type continuity conditions apply at the domain boundaries. When $N = 1$, there are no intergranular interactions; the Taylor model may thus be denoted either as the $\mathscr{E}^1$ or $\mathscr{S}^1$ model. Also, in the present notation $\mathscr{E}^2$ represents the 'ALAMEL' model. As noted previously in Sec. 2, each stack of N domains obeys the Taylor hypothesis, i.e., macroscopic deformation $\boldsymbol{L}^{\text{imp}}$ is imposed upon it as a whole.

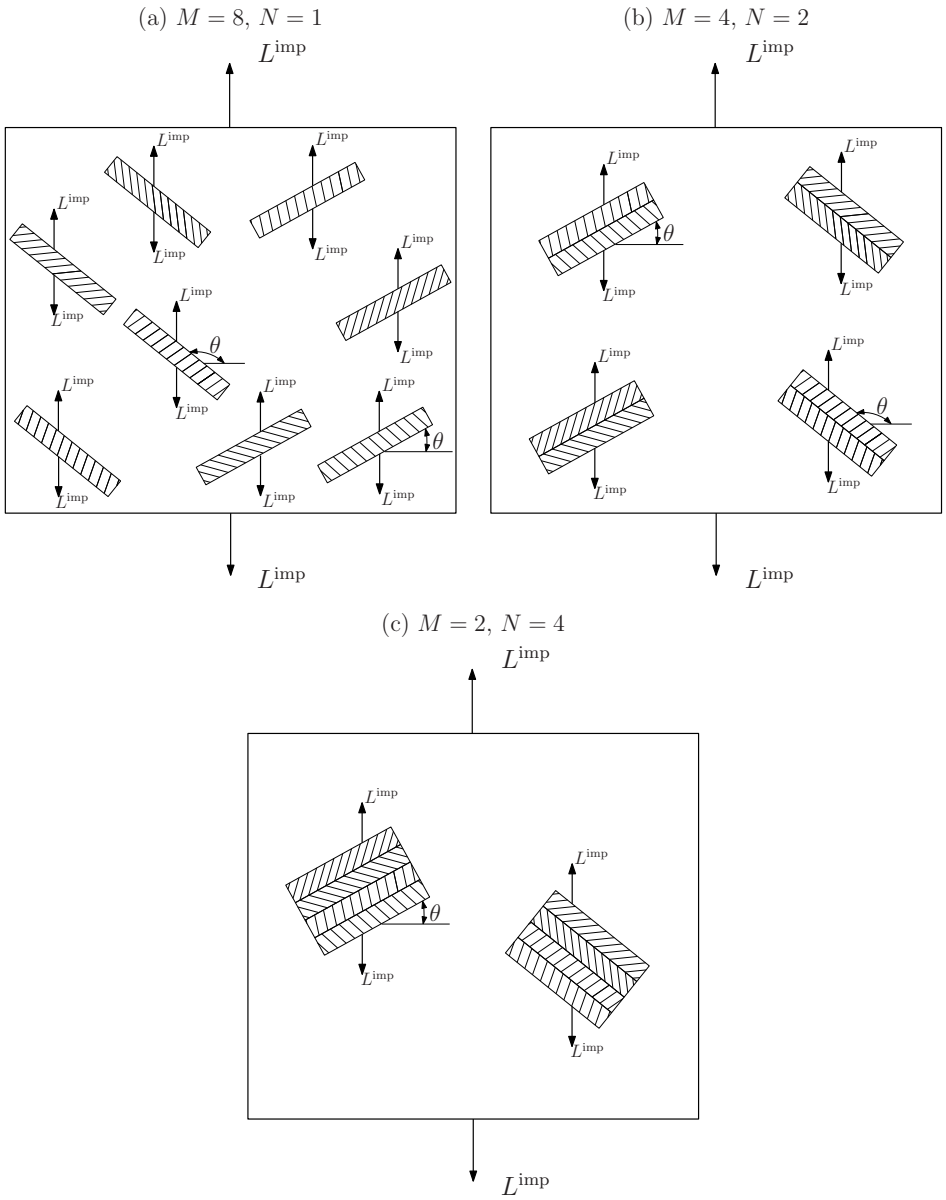

Fig. 5. Three possible representations of an $n_g = 8$ domain polycrystalline aggregate by (a) $\mathscr{E}^1$, (b) $\mathscr{E}^2$ and (c) $\mathscr{E}^4$ models.

Polycrystal response to two types of imposed macroscopic deformation,

$$[\boldsymbol{L}^{\text{imp}}]_{xy} = \begin{bmatrix} -1 & 0 \\ 0 & 1 \end{bmatrix}, \tag{65}$$

which represents plane strain tension in the y-direction and

$$[\boldsymbol{L}^{\mathrm{imp}}]_{xy} = \begin{bmatrix} 0 & 1 \\ \\ 0 & 0 \end{bmatrix} \tag{66}$$

which represents simple shear in the xy-plane, are studied.

4.1 Stress-strain response

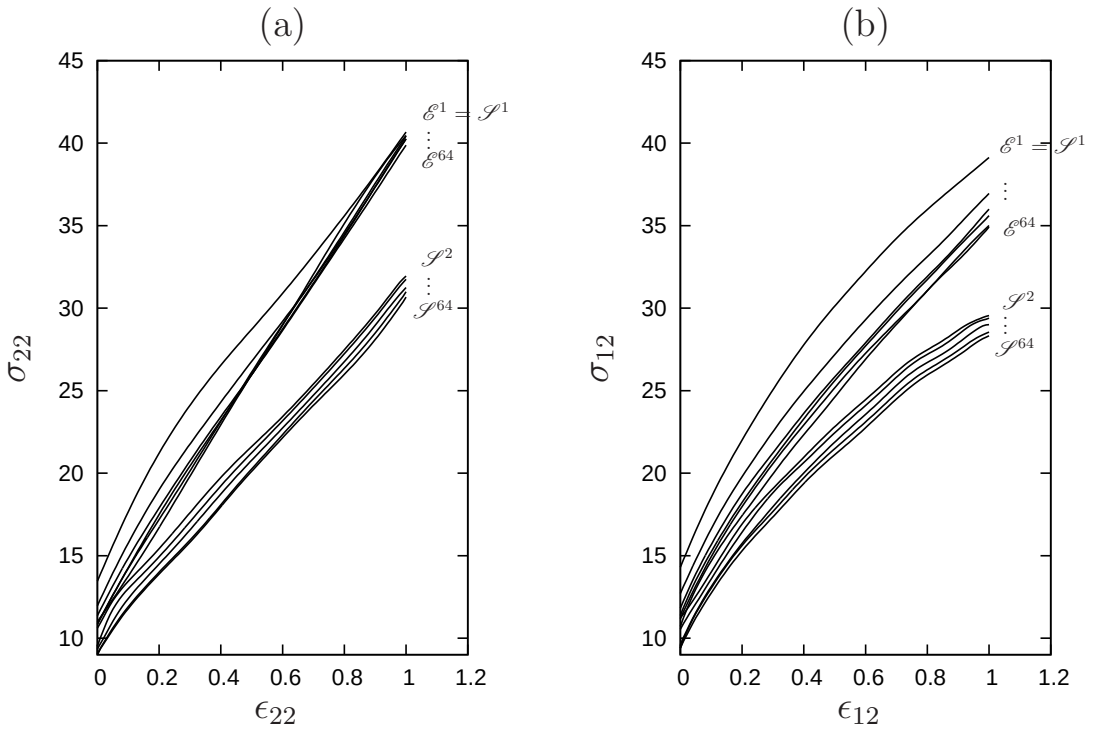

Fig. 6. Macroscopic stress-strain response predicted by $\mathscr{E}^N$ and $\mathscr{S}^N$ models of the same $n_g = 1024$ domain two-dimensional polycrystalline aggregate for $N = 1$, $N = 2$, $N = 4$, $N = 8$ and $N = 16$ under (a) tension and (b) simple shear. Model $\mathscr{E}^1 = \mathscr{S}^1$ is the Taylor model and model $\mathscr{E}^2$ is the 'ALAMEL' model.

Figs. 6a and b show the macroscopic stress-strain response obtained in tension

and simple shear, respectively, from $\mathscr{E}^N$ and $\mathscr{S}^N$ models of the same 1024 domain polycrystalline aggregate for $N = 1, 2, 4, 8, 16$. It is seen that the macroscopic response of all $\mathscr{E}^N$ models is harder than that of any of the $\mathscr{S}^N$ models and even within one domain boundary continuity condition type, $\mathscr{E}^N$ or $\mathscr{S}^N$, the macroscopic response hardens with decreasing N. The Taylor model ($\mathscr{E}^1$ or $\mathscr{S}^1$) predicts the hardest response of all models considered, followed by the 'ALAMEL' model ($\mathscr{E}^2$).

It is also seen from Figs. 6a and b that amongst the $\mathscr{E}^N$ models where velocity continuity is enforced at the domain boundaries, the predicted macroscopic stress-strain response saturates at about $N = 4$. That is, further softening of the macroscopic stress-strain response under both tensile and simple shear loading occurs for $N \geq 4$, but is not substantial. Amongst the $\mathscr{S}^N$ models however, the predicted macroscopic stress-strain curve shows sustained diminution with increasing N.

Softening of the stress-strain response with increasing N appears to derive from diminished constraints imposed on individual domains that are part of a larger 'stack'. Figs. 6a and b suggest that constraints on individual domains decrease with increasing N in both $\mathscr{E}^N$ and $\mathscr{S}^N$-models. Further, suppressing the requirement of velocity continuity across domain boundaries, Eq. (52), in the $\mathscr{S}^N$ models appears to reduce constraints on domains further still, and result in a macroscopic response softer than that of the $\mathscr{E}^N$-models. Constraint reduction appears to saturate beyond about $N \geq 4$ in the $\mathscr{E}^N$ models, while proceeding without saturation in the $\mathscr{S}^N$-models. Examining the slip system activity in domains provides a means to verify the foregoing qualitative statements.

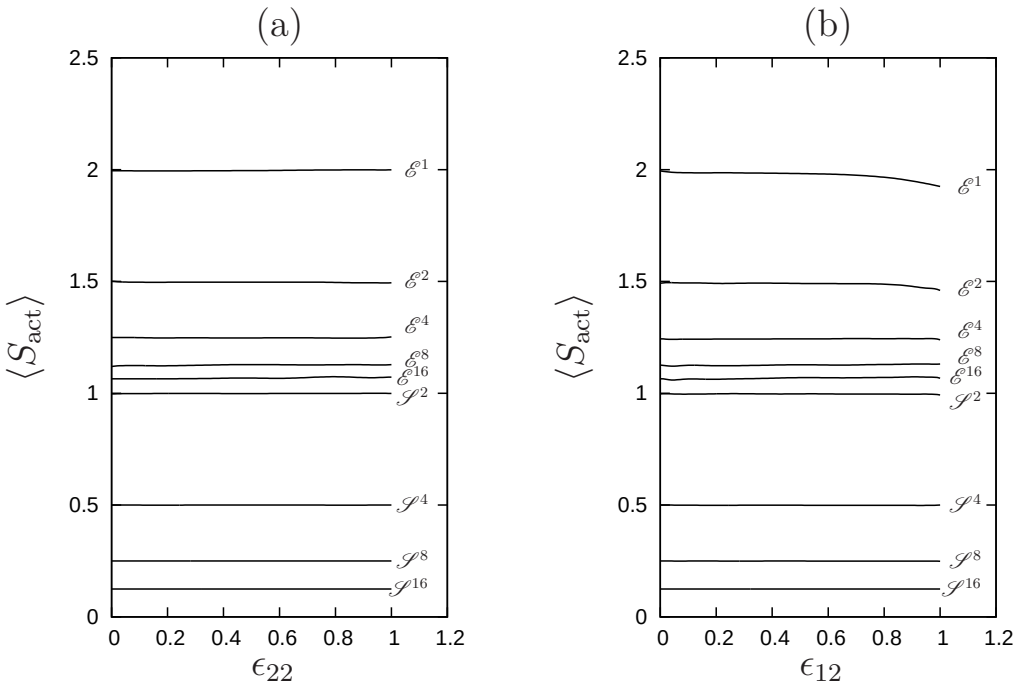

Fig. 7. Evolution of the average number of active slip systems, $\langle S_{\rm act} \rangle$ for different size sub-aggregates subjected to (a) tension and (b) simple shear. Curves $\mathscr{E}^1, \ldots, \mathscr{E}^{16}$ were obtained by assuming $\mathscr{E}$-type intergranular constraints given by Eq. (51) and curves $\mathscr{S}^1, \ldots, \mathscr{S}^{16}$ assume $\mathscr{S}$-type intergranular constraints given by Eq. (52).

Quantitative understanding of the diminution of constraints with increasing sub-aggregate size N can be obtained by considering the average number of activated slip-systems

$$\langle S_{\rm act} \rangle = \sum_{g=1}^{N} \rho^{[g]} \sum_{s=1}^{S} 1_{[\dot{\gamma}_s^{[g]} > 0]}. \tag{67}$$

Here, $1_{[\dot{\gamma}_s^{[g]} > 0]}$ is the indicator function of the condition $\dot{\gamma}_s^{[g]} > 0$.

A domain in the Taylor model $\mathscr{E}^1 = \mathscr{S}^1$ will require activation of both slip systems to accommodate arbitrary imposed deformation. This is the case throughout the tensile deformation as shown by Fig. 7a. When subjected to simple shear deformation, Taylor domains rotate into an orientation wherein a single slip direction is aligned with the shear direction. This reduces the number of slip systems activated in suitably oriented Taylor domains and causes a drop in $\langle S_{\text{act}} \rangle$, as seen in Fig. 7b.

$\langle S_{\text{act}} \rangle$ of both $\mathscr{E}^N$ and $\mathscr{S}^N$ models decrease with increasing N. This supports the explanation of Sec. 4.1 for the softer mechanical response obtained with larger N. In the $\mathscr{E}^N$ models, $\langle S_{\text{act}} \rangle > 1$, always, i.e., on average, at least one slip system is active in each domain to accommodate the inter-granular continuity constraint. Insignificant reduction in $\langle S_{\text{act}} \rangle$ occurs for $N \geq 4$, which explains the saturation of the stress-strain curves in Fig. 6.

In the case of the $\mathscr{S}^N$ models, wherein no compatibility is demanded across domain boundaries, $\langle S_{\text{act}} \rangle$ drops below 1 for $N > 2$. Thus, some of the domains in the 'stack' do not deform at all. In fact, of the $2N$ slip systems in a stack of N domains, only two need be active in an $\mathscr{S}^N$ model to accommodate the imposed deformation. This implies that $\langle S_{\text{act}} \rangle = 2/N$. It is seen from Fig. 7 that this value agrees with the $\langle S_{\text{act}} \rangle$ calculated from the simulations. Substantial diminution of $\langle S_{\text{act}} \rangle$, and hence the macroscopic stress-strain response obtained from the $\mathscr{S}^N$ models continues beyond $N = 4$: its predictions are hence slower to saturate than those of the $\mathscr{E}^N$ models. The $\mathscr{S}^{n_g}$ model defines the lower bound of the mechanical response amongst all $\mathscr{S}^N$ models. It coincides with the lower bound model of Sachs (1928).

4.3 Texture evolution

Since the lattice orientation of a domain can be specified by single scalar, ω, two-dimensional polycrystal texture is amenable to simpler representation by means of histograms instead of the usual pole figure or orientation distribution space representations. Figs. 8 and 9 show texture evolution in this format in the $n_g = 1024$ domain polycrystal subjected to tensile and shear deformations, respectively. The initial random distribution of lattice orientations in both cases are the same and are shown in Fig. 8a and Fig. 9a. Rows b, c, d and e in these figures show texture evolution in the $\mathscr{E}^1$ (Taylor), $\mathscr{E}^2$ ('ALAMEL'), $\mathscr{E}^4$ and $\mathscr{E}^{16}$ models, respectively. Columns 1, 2 and 3 of rows b, . . ., e show texture snapshots at characteristic strain levels (ϵ_{22} for tension and ϵ_{12} for shear) of 0.25, 0.50 and 1.00.

Qualitative predictions of texture evolution under tensile deformation of all the $\mathscr{E}^N$ models are similar for $N = 1, 2, 4$ and 16. domains in all the models rotate toward the stable orientation in tension at $\omega^* = 90^\circ$ at which both slip systems are inclined 30° to the tensile axis. Quantitatively, however, the rates of rotation are very different. Thus, when the imposed axial strain, $\epsilon_{22} = 1.00$, the volume fraction of the domains within 5° of ω^* is largest for the $\mathscr{E}^1$ Taylor model (86%) and decreases progressively with increasing N: The fraction of domains within 5° of ω^* are 68% for $\mathscr{E}^2$, 63% for $\mathscr{E}^4$, 59% for $\mathscr{E}^8$, 54% for $\mathscr{E}^{16}$ and 54% for $\mathscr{E}^{64}$. Thus, the texture intensity around ω^* after a fixed strain ϵ_{22} decreases with increasing N, but saturates with increasing N. Normalizing by the volume fraction in the $\mathscr{E}^{64}$ model, we obtain $\mathscr{E}^1 : \mathscr{E}^2 : \mathscr{E}^4 : \mathscr{E}^8 : \mathscr{E}^{16} : \mathscr{E}^{64} = 1.59 : 1.26 : 1.17 : 1.09 : 1.00 : 1.00$. The $\mathscr{E}^{16}$ model thus suffices to approximate long-range intergranular interactions to the second decimal place

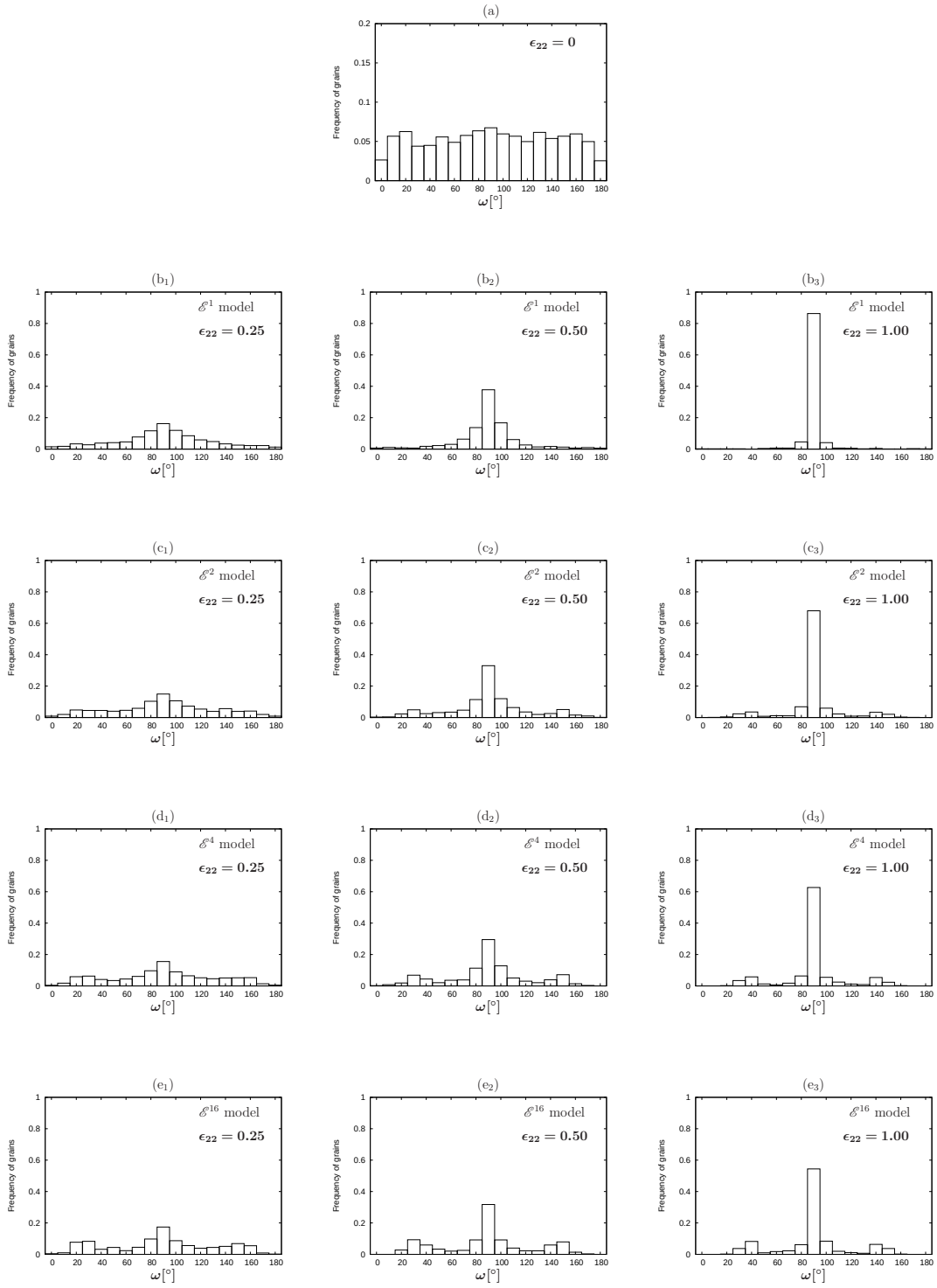

Fig. 8. Texture evolution of model polycrystals subjected to imposed macroscopic tensile deformation given by Eq. (65). Row a shows the initial random texture. Rows b – e show texture evolution in the $\mathscr{E}^1$ (Taylor), $\mathscr{E}^2$ ('ALAMEL'), $\mathscr{E}^4$ and $\mathscr{E}^{16}$ models, respectively. Columns 1, 2 and 3 show texture snapshots at strain levels ϵ_{22} of 0.25, 0.50 and 1.00.

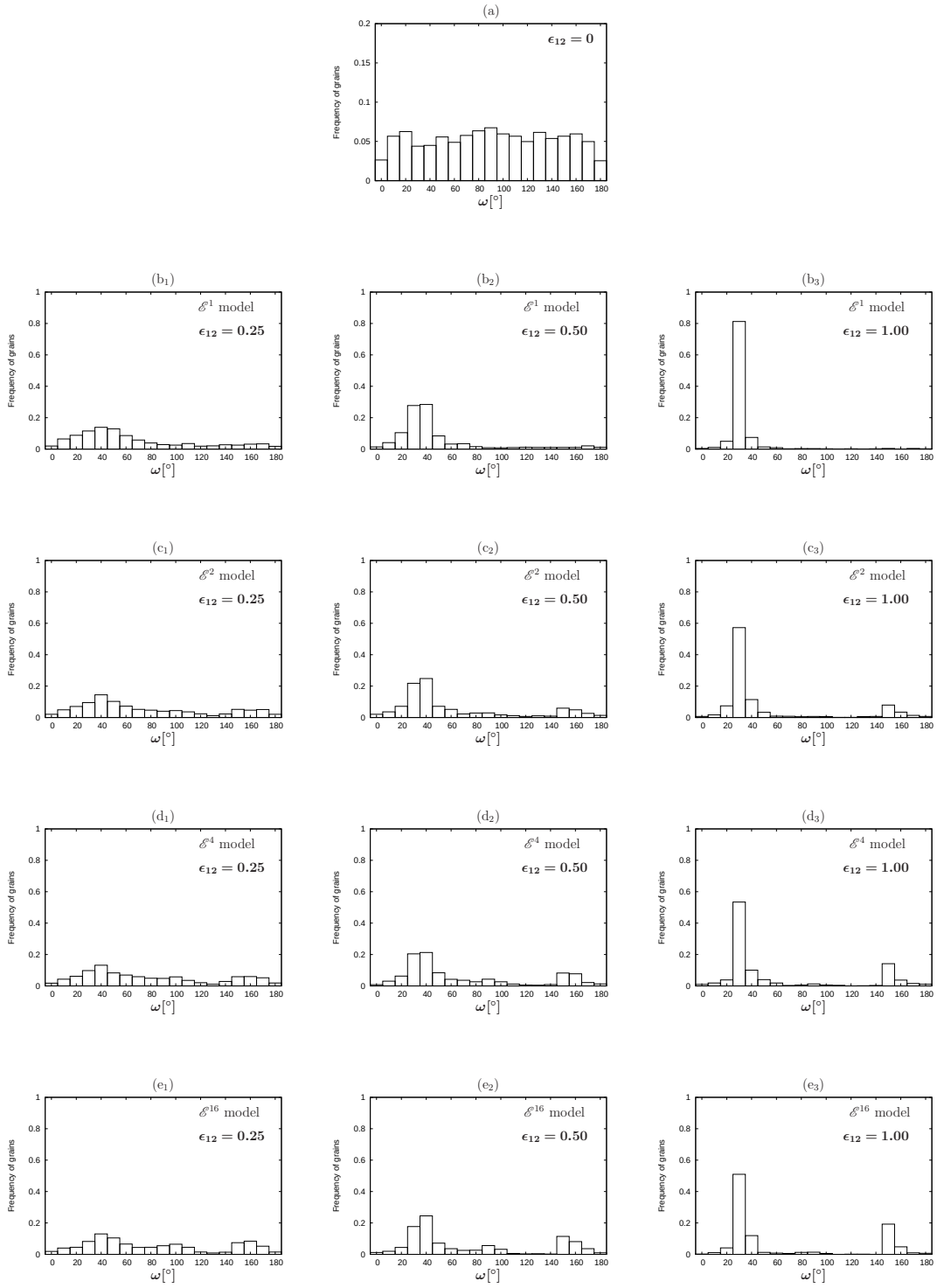

Fig. 9. Texture evolution of model polycrystals subjected to imposed macroscopic simple shear deformation given by Eq. (66). Row a shows the initial random texture. Rows b – e show texture evolution in the $\mathscr{E}^1$ (Taylor), $\mathscr{E}^2$ ('ALAMEL'), $\mathscr{E}^4$ and $\mathscr{E}^{16}$ models, respectively. Columns 1, 2 and 3 show texture snapshots at strain levels ϵ_{12} of 0.25, 0.50 and 1.00.

of texture intensity ratio.

In contrast with tension, predicted texture evolution under shear deformation differs both qualitatively and quantitatively amongst the various $\mathscr{E}^N$ models. The stable orientation in simple shear corresponds to $\omega^* = 30°$, wherein the $\boldsymbol{n}_s$ and $\boldsymbol{b}_s$ of one of the two slip systems coincides with the macroscopic shear plane normal and shear direction, respectively. Such coincidence is also possible at $\omega = 150°$. This, however, does not represent a stable orientation, as Taylor domains given small perturbations about $\omega = 150°$ also rotate toward $\omega^* = 30°$. Thus, the texture predicted by the Taylor $\mathscr{E}^1$ model at $\epsilon_{12} = 1.00$ shown in Fig. 9b$_3$ shows most of the domains (81%) oriented within 5° of $\omega^* = 30°$ and hardly any domains oriented close to $\omega = 150°$. However, intergranular interactions in the $\mathscr{E}^N$ models, for $N \geq 2$ stabilize the $\omega = 150°$ orientation as well. The texture intensity around $\omega = 150°$ increases with increasing N: 0.4% for $\mathscr{E}^1$, 8% for $\mathscr{E}^2$, 14% for $\mathscr{E}^4$, 18% for $\mathscr{E}^8$, 19% for $\mathscr{E}^{16}$ and 20% for $\mathscr{E}^{64}$. These intensities are comparable to those around the Taylor stable end orientation of $\omega^* = 30°$: In the $\mathscr{E}^{64}$ model, the volume fraction within 5° of $\omega = 150°$ is significant (20%) and about 40% of that around $\omega^* = 30°$ (51%). We conclude that accounting for intergranular interactions results in qualitatively different predicted textures amongst the various $\mathscr{E}^N$ models.

Quantitative differences between the models also appear during simple shear deformation. Paralleling the reduction in the rate of lattice rotation during tensile deformation, we find that the volume fraction concentrated within 5° of $\omega^* = 30°$ decreases, but saturates with increasing N of the $\mathscr{E}^N$ models: The fraction of domains within 5° of ω^* are 81% for $\mathscr{E}^1$, 57% for $\mathscr{E}^2$, 53% for $\mathscr{E}^4$, 52% for $\mathscr{E}^8$, 51% for $\mathscr{E}^{16}$ and 51% for $\mathscr{E}^{64}$. Normalizing by the volume fraction of domains within 5° of ω^*, as predicted by the $\mathscr{E}^{64}$ model, we find

$\mathscr{E}^1 : \mathscr{E}^2 : \mathscr{E}^4 : \mathscr{E}^8 : \mathscr{E}^{16} : \mathscr{E}^{64} = 1.59 : 1.12 : 1.04 : 1.02 : 1.00 : 1.00$. Thus, in simple shear too, as in tension, the texture intensity at ω^* decreases but saturates with increasing N. Considering intensities around both $\omega = 30°$ and $\omega = 150°$, we find as before, that the $\mathscr{E}^{16}$ model suffices to approximate long-range intergranular interactions to the second decimal place of texture intensity ratio.

The present work has demonstrated the importance of accounting for inter-domain interactions in texture prediction in a hypothetical two-dimensional polycrystal. Application of the model to predict texture evolution in three-dimensional polycrystals and quantitative comparison of the textures predicted with various models, and that obtained from experiment, following Van Houtte et al. (2004), Van Houtte et al. (2006), is left for future work. It is also left to future work to determine the sensitivity of the predicted mechanical response and texture evolution to the representation of the microstructure in terms of stacks of domains discussed in connection with Fig. 1.

5 Computational time

All simulations reported in the present work were carried out a typical PC with a 2.27 GHz processor. Fig. 10 shows the wall clock computational time per domain required to simulate tensile deformation up to strain $\epsilon_{22} = 1.0$ and simple shear deformation up to strain $\epsilon_{12} = 1.0$ using the $\mathscr{E}^N$ models of a polycrystal for $N = 1, 2, 4, 8, 16$ and 64. As expected, simulation times increase with N as the models consider longer range intergranular interactions with increasing N. Notably, however, computational times grow sub-linearly with N. Also, computational times for any of the $\mathscr{E}^N$ models considered is

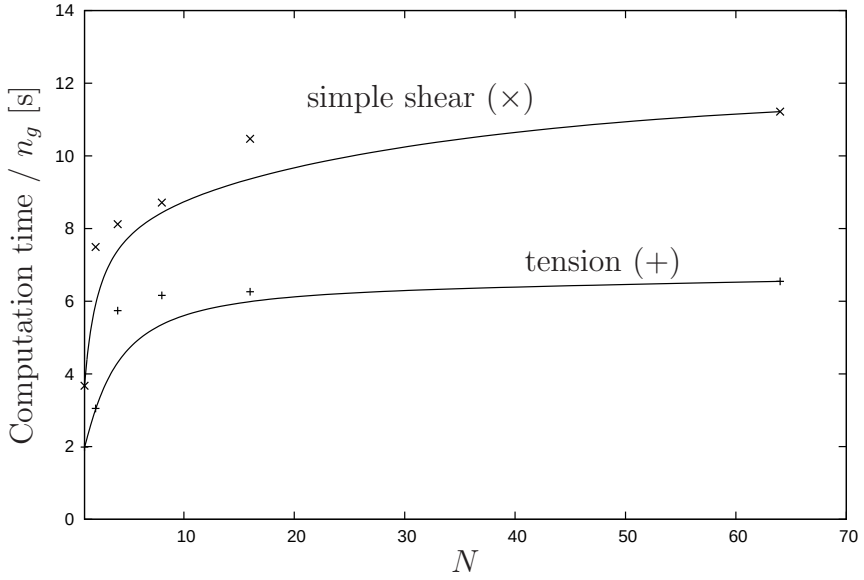

Fig. 10. Total computational time per domain required to simulate tensile deformation to strain $\epsilon_{22} = 1$ (+) and simple shear deformation to strain $\epsilon_{12} = 1$ (×). Since the data is noisy, smooth curves associated with each of the two data sets are also shown to assist in their interpretation.

within a factor of four of the corresponding Taylor $\mathscr{E}^1$ model.

We also find that implementation of the consistency conditions described in Sec. 2.2.5 reduces computational time substantially. This is because, enforcing consistency reduces the degree of non-uniqueness, or often even eliminates non-uniqueness of the solution. This extends the length of time steps of the adaptive integration method used.

The reduction in computational time increases with increasing N. In simulating tension to strain $\epsilon_{22} = 1.00$, the computational time when enforcing consistency is reduced by 0% for $\mathscr{E}^1$, 19% for $\mathscr{E}^2$, 21% for $\mathscr{E}^4$, 22% for $\mathscr{E}^8$ and 45% for $\mathscr{E}^{16}$ from its value without enforcing the consistency conditions. No reduction is obtained in the Taylor case ($\mathscr{E}^1$) because excepting special orientations, the solution to the deformation problem is already unique.

6 Conclusion

A 'stack' model that accounts for intergranular interactions between N domains abutting each other has been proposed. It extends the 'ALAMEL' models of Van Houtte et al. (2005) which treats interactions between pairs of neighboring domains. Allowing for interaction between multiple domains has been shown to reduce the constraint on individual domains, i.e., soften the predicted stress-strain response, reduce the number of activated slip systems per domain. This produces qualitative and quantitative differences in the predicted texture when used to simulate tensile and simple shear deformations of a model two-dimensional polycrystal. All the observed responses, both macroscopic and microscopic, saturate with increasing N. Furthermore, the computational time associated with the present model increases only sublinearly with increasing N.

As stated in Sec. 1, successful multi-scale numerical simulations of deformation processes pose conflicting requirements of quantitative accuracy in the predicted macroscopic response and microscopic state, as well as computational lightness of the micro-scale model. In the 'stack' model, the conflict between these requirements appears to be within manageable limits. As seen previously, for a specified degree of accuracy of the stress-strain and texture response, an appropriate $\mathscr{E}^N$ model capable of supplying response to that accuracy can be identified whose computational cost will be well within an order of magnitude of that required for the Taylor model. Although these conclusions have been arrived by studying a two-dimensional polycrystal, their applicability to three-dimensional polycrystals also appears likely. The present 'stack' model is thus ideally suited for the purpose of supplying material point

response in simulations of macroscopic plastic deformation processes.

Acknowledgment: The authors thank the anonymous referees of this manuscript for suggestions that helped improve it. Funding for this work was provided by the Indira Gandhi Center for Atomic Research, Kalpakkam.

References

Aernoudt, E., Van Houtte, P., Leffers, T., 1993. Plastic Deformation and Fracture of Materials. Vol. 6 of Materials Science and Technology: A Comprehensive Treatment. VCH, Ch. Deformation and textures of metals at large strains, pp. 89–136.

Amirkhizi, A. V., Nemat-Nasser, S., 2007. A framework for numerical integration of crystal elasto-plastic constitutive equations compatible with explicit finite element codes. Int. J. Plast. 23 (10-11), 1918–1937.

Anand, L., Kothari, M., 1996. A computational procedure for rate-independent crystal plasticity. J. Mech. Phys. Solids 44 (4), 525–558.

Asaro, R., Lubarda, V., 2006. Mechanics of Solids and Materials. Cambridge University Press.

Asaro, R. J., 1979. Geometrical effects in the inhomogeneous deformation of ductile single crystals. Acta metall. 27 (3), 445–453.

Asaro, R. J., 1983. Micromechanics of crystals and polycrystals. In: Hutchinson, J. W., Wu, T. Y. (Eds.), Advances in Applied Mechanics. Vol. 23. Academic Press, New York, Ch. 1, pp. 1–115.

Ashby, M. F., 1970. The deformation of plastically non-homogeneous materials. Phil. Mag. 21 (170), 399.

Barbe, F., Decker, L., Jeulin, D., Cailletaud, G., 2001. Intergranular and in-

tragranular behavior of polycrystalline aggregates. part 1: F.E. model. Int. J. Plast. 17 (4), 513–536.

Barrett, C. S., Levenson, L. H., 1940. Structure of aluminum after compression. Trans. AIME 137, 112–127.

Barton, N. R., Knap, J., Arsenlis, A., Becker, R., Hornung, R. D., Jefferson, D. R., 2008. Embedded polycrystal plasticity and adaptive sampling. Int. J. Plast. 24 (2), 242–266.

Beaudoin, A. J., Dawson, P. R., Mathur, K. K., Kocks, U. F., 1995. A hybrid finite element formulation for polycrystal plasticity with consideration of macrostructural and microstructural linking. Int. J. Plast. 11 (5), 501–521.

Beaudoin, A. J., Mathur, K. K., Dawson, P. R., Johnson, G. C., 1993. Three-dimensional deformation process simulation with explicit use of polycrystal plasticity models. Int. J. Plast. 9 (7), 833–860.

Bishop, J. F. W., Hill, R., 1951. A theory of the plastic distortion of a polycrystalline aggregate under combined stresses. Phil. Mag. 42 (327), 414–427.

Bystrzycki, J., Kurzydlowski, K. J, Przetakiewicz, W., 1997. On the geometry of twin boundaries and their contribution to the strengthening and recovery of FCC polycrystals. Mater. Sci. Eng. A 225, 188-195.

Chin, G. Y., Mammel, W. L., 1969. Generalization and equivalence of the minimum work (Taylor) and Maximum work (Bishop-Hill) Principles of Crystal Plasticity. Trans. AIME 245, 1211.

Christoffersen, H., Leffers, T., 1997. The orientation of dislocation walls in rolled copper relative to the crystallographic coordinate system. Scripta mater. 37 (12), 2041–2046.

Cuitiño, A. M., Ortiz, M., 1992. Computational modeling of single crystals. Modelling Simul. Mater. Sci. Eng. 1, 225–263.

Engler, O., Crumbach, M., Li, S., 2005. Alloy-dependent rolling texture sim-

ulation of aluminium alloys with a grain-interaction model. Acta mater. 53 (8), 2241–2257.

Fleck, N. A., Ashby, M. F., Hutchinson, J. W., 2003. The role of geometrically necessary dislocations in giving material strengthening. Scripta mater. 48, 179–183.

Fuh, S., Havner, K. S., 1986. On uniqueness of multiple-slip solutions in constrained and unconstrained f.c.c. crystal deformation problems. International Journal of Plasticity 2 (4), 329–345.

Ganapathysubramanian, S., Zabaras, N., 2005. Modeling the thermoelastic-viscoplastic response of polycrystals using a continuum representation over the orientation space. Int. J. Plast. 21 (1), 119–144.

Garmestani, H., Lin, S., Adams, B. L., Ahzi, S., 2001. Statistical continuum theory for large plastic deformation of polycrystalline materials. J. Mech. Phys. Solids 49 (3), 589–607.

Guan, Y., Pourboghrat, F., Barlat, F., 2006. Finite element modeling of tube hydroforming of polycrystalline aluminum alloy extrusions. Int. J. Plast. 22 (12), 2366–2393.

Gurtin, M. E., 1981. An introduction to continuum mechanics. Academic Press, New York.

Haddadi, H., Bouvier, S., Banu, M., Maier, C., Teodosiu, C., 2006. Towards an accurate description of the anisotropic behaviour of sheet metals under large plastic deformations: Modelling, numerical analysis and identification. Int. J. Plast. 22 (12), 2226–2271.

Havner, K. S., 1992. Finite Plastic Deformation of Crystalline Solids. Cambridge University Press.

Havner, K. S., Chidambarrao, D., 1987. Analysis of a family of unstable lattice orientations in (110) channel die compression. Acta mech. 69 (1-4), 243–269.

Hill, R., 1961. Discontinuity relations in mechanics of solids. In: Sneddon, I. N., Hill, R. (Eds.), Progress in Solid Mechanics. Vol. 2. Interscience Publishers, New York, Ch. 6, pp. 247–278.

Hill, R., 1966. Generalized constitutive relations for incremental deformation of metal crystals by multislip. J. Mech. Phys. Solids 14 (2), 95–102.

Hirsch, J., Lucke, K., 1988a. Mechanism of deformation and development of rolling textures in polycrystalline FCC metals: I Description of rolling texture in homogeneous CuZn alloys. Acta metall. 36 (11), 2863–2882.

Hirsch, J., Lucke, K., 1988b. Mechanism of deformation and development of rolling textures in polycrystalline FCC metals: II Simulation and interpretation of experiments on the basis of Taylor-type theories. Acta metall. 36 (11), 2883–2904.

Honneff, H., Mecking, H., 1978. A method for the determination of the active slip systems and orientation changes during single crystal deformation. In: Proc. 5th Int. Conf. on the Textures of Materials. Vol. 1. Springer-Verlag, pp. 265–275.

Kalidindi, S. R., Bronkhorst, C. A., Anand, L., 1992. Crystallographic texture evolution in bulk deformation processing of FCC metals. J. Mech. Phys. Solids, 537–569.

Kalidindi, S. R., Duvvuru, H. K., 2005. Spectral methods for capturing crystallographic texture evolution during large plastic strains in metals. Acta mater. 53 (13), 3613–3623.

Kalidindi, S. R., Duvvuru, H. K., Knezevic, M., 2006. Spectral calibration of crystal plasticity models. Acta Mater. 54 (7), 1795–1804.

Kanjarla, A. K., Van Houtte, P., Delannay, L., 2010. Assessment of plastic heterogeneity in grain interaction models using crystal plasticity finite element method. Int. J. Plast. 26, 1220–1233.

Kim, J. H., Lee, M.-G., Barlat, F., Wagoner, R. H., Chung, K., 2008. An elasto-plastic constitutive model with plastic strain rate potentials for anisotropic cubic metals. Int. J. Plast. 24 (12), 2298–2334.

Knezevic, M., Kalidindi, S. R., Fullwood, D., 2008. Computationally efficient database and spectral interpolation for fully plastic Taylor-type crystal plasticity calculations of face-centered cubic polycrystals. Int. J. Plast. 24, 1264–1276.

Kocks, U. F., Canova, G. R., 1981. How many slip systems, and which? In: et al, N. H. (Ed.), Deformation of Polycrystals. Vol. 2. Riso National Laboratory, Roskilde, Denmark, p. 135.

Kocks, U. F., Chandra, 1982. Slip geometry in partially constrained deformation. Acta Metall. 30 (3), 695–709.

Kocks, U. F., Tomé, C. N., Wenk, H. R., 1998. Texture and Anisotropy. Cambridge University Press, Cambridge, U.K.

Le, N. T., Havner, K. S., 1985. Analysis of tensile loaded f.c.c. crystals in 4- and 8-fold symmetry. Mechanics of Materials 4 (1), 33–50.

Lebensohn, R., 1999. Modeling the role of local correlations in polycrystal plasticity using viscoplastic self-consistent schemes. Modeling Simul. Mater. Sci. Eng. 7, 739–746.

Lebensohn, R., Ühlenhut, H., Hartig, C., Mecking, H., 1998a. Plastic flow of γ-TiAl-based polysynthetically twinned crystals: micromechanical modeling, and experimental validation. Acta mater. 46 (13), 4701–4709.

Lebensohn, R. A., Turner, P. A., Signorelli, J. W., Canova, G. R., Tomé, C. N., 1998b. Calculation of intergranual stresses based on a large strain visoplastic self-consistent polycrystal model. Modelling Simul. Mater. Sci. Eng. 6, 447–465.

Lebensohn, R. E., Tomé, C. N., 1993. A self-consistent anisotropic approach for

the simulation of plastic deformation and texture development of polycrystals: application to zirconium alloys. Acta metall. mater. 41 (9), 2611–2624.

Lee, B. J., Ahzi, S., Parks, D. M., 2002. Bicrystal-based modeling of plasticity in FCC metals. J. Eng. Mater. Tech. 124 (1), 27.

Lee, E. H., 1969. Elastic-plastic deformation at finite strains. J. Appl. Mech. 36, 1–6.

Leffers, T., 1975. On the misfit between the grains in a deformed sachs polycrystal and its relation to the inhomogeneous deformation of real polycrystals. Scripta metall. 9, 261–264.

Leffers, T., 1978. The shortcomings of the Taylor model in the description of the plastic deformation of real polycrystals. In: Proc. 5th Int. Conf. on the Textures of Materials. Vol. 1. Springer-Verlag, pp. 277–287.

Leffers, T., Christoffersen, H., 1997. The importance of grain-to-grain interaction during rolling deformation of copper. Mater. Sci. Eng. A234–236, 676–679.

Liu, Q., Hansen, N., 1998. Macroscopic and microscopic subdivision of a cold-rolled aluminium single crystal of cubic orientation. Proc. R. Soc. Lond. A 454, 2555–2592.

Logé, R. E., Chastel, Y. B., 2006. Coupling the thermal and mechanical fields to metallurgical evolutions within a finite element description of a forming process. Comput. Method. Appl. Mech. 195 (48-49), 6843–6857.

Mahesh, S., 2006. Deformation banding and shear banding in single crystals. Acta mater. 54 (17), 4565–4574.

Mahesh, S., 2009. A hierarchical model for rate-dependent polycrystals. Int. J. Plast. 25 (5), 752–767.

Mahesh, S., 2010. A binary tree based model for rate-independent polycrystals. Int. J. Plast. 26 (1), 42–64.

Mahesh, S., Tomé, C. N., McCabe, R. J., Kaschner, G. C., Beyerlein, I. J., Misra, A., 2004. Application of a sub-structure based hardening model to copper under loading path changes. Metall Mater Trans A 35, 3763–3774.

Manonukul, A., Dunne, F. P. E., 2004. High- and low-cycle fatigue crack initiation using polycrystal plasticity. Proc. R. Soc. A 460 (2047), 1881–1903.

Mathur, K. K., Dawson, P. R., 1989. On modeling the development of crystallographic texture in bulk forming processes. Int. J. Plast. 5 (1), 67–94.

Mika, D. P., Dawson, P. R., 1998. Effects of grain interaction on deformation in polycrystals. Mater. Sci. Eng. A 257 (1), 62–76.

Molinari, A., Canova, G. R., Ahzi, S., 1987. A self consistent approach of the large deformation polycrystal viscoplasticity. Acta metall. 35, 2983–2994.

Paul, H., Morawiec, A., Driver, J. H., Bouzy, E., 2009. On twinning and shear banding in a Cu8 at.% Al alloy plane strain compressed at 77K. Int. J. Plasticity 25, 1588–1608.

Peeters, B., Bacroix, B., Teodosiu, C., Houtte, P. V., Aernoudt, E., 2001a. Work-hardening/softening behavior of bcc polycrystals during changing strain paths: II TEM observations of dislocation sheets in an if steel during two-stage strain paths and their representation in terms of dislocation densities. Acta Mater. 49, 1621–1632.

Peeters, B., Seefeldt, M., Teodosiu, C., Kalidindi, S. R., Houtte, P. V., Aernoudt, E., 2001b. Work-hardening/softening behavior of bcc polycrystals during changing strain paths: I An integrated model based on substructure and texture evolution, and its prediction of the stress-strain behavior of an IF steel during two-stage strain paths. Acta Mater. 49, 1607–1619.

Pierce, D., Asaro, R. J., Needleman, A., 1983. Material rate dependence and localized deformation in crystalline solids. Acta metall. 31 (12), 1951–1976.

Proust, G., Tomé, C. N., Kaschner, G. C., 2007. Modeling texture, twinning

and hardening evolution during deformation of hexagonal materials. Acta mater. 55, 2137–2148.

Radhakrishnan, K., Hindmarsh, A. C., 1993. Description and use of lsode, the livermore solver for ordinary differential equations. In: Hindmarsh, A. C. (Ed.), Lawrence Livermore National Laboratory. NASA reference publication, CA, USA, pp. 1–124.

Renouard, M., Wintenberger, M., 1981. Determination de l'amplitude des glissements dans la deformation plastique homogene d'un monocristal sous l'effet de contraintes et de diplacements imposes. C. R. Acad. Sci 283, 385–388.

Rice, J. R., 1971. Inelastic constitutive relations for solids: An internal-variable theory and its application to metal plasticity. J. Mech. Phys. Solids 19 (6), 433–455.

Sachs, G., 1928. Zur Ableitung einer Fliessbedingung. Z. Ver. Dtsch. Ing. 72, 734–736.

Taylor, G. I., 1938. Plastic strain in metals. J. Inst. Met. 62, 307.

Tomé, C., Canova, G. R., Kocks, U. F., Christodoulou, N., Jonas, J. J., 1984. The relation between macroscopic and microscopic strain hardening in F.C.C polycrystals. Acta metall. 32 (10), 1637–1653.

Van Houtte, P., 1982. On the equivalence of the relaxed Taylor theory and the Bishop-Hill theory for partially constrained plastic deformation of crystals. Mater. Sci. Engng. 55, 69–77.

Van Houtte, P., Aernoudt, E., 1975a. Solution of the generalized Taylor theory of plastic flow. I and II. Z. Metallkde. 66, 202–209.

Van Houtte, P., Aernoudt, E., 1975b. Solution of the generalized Taylor theory of plastic flow. III Applications. Z. Metallkde. 66, 303–306.

Van Houtte, P., Delannay, L., Kalidindi, S. R., 2002. Comparison of two grain

interaction models for polycrystal plasticity and deformation texture prediction. Int. J. Plast. 18 (3), 359–377.

Van Houtte, P., Delannay, L., Samajdar, I., 1999. Quantitative predictions of the cold-rolling texture in low-carbon steel by means of the LAMEL model. Texture microstruct 31 (3), 104–119.

Van Houtte, P., Kanjarla, A. K., Van Bael, A., Seefeldt, M., Delannay, L., 2006. Multiscale modelling of the plastic anisotropy and deformation texture of polycrystalline materials. Eur J Mech. A 25 (4), 634–648.

Van Houtte, P., Li, S., Engler, O., 2004. Modelling deformation texture of aluminium alloys using grain interaction models. Aluminium 80, 702–706.

Van Houtte, P., Li, S., Seefeldt, M., Delannay, L., 2005. Deformation texture prediction: from the Taylor model to the advanced lamel model. Int. J. Plast. 21 (3), 589–624.

Van Houtte, P., Yerra, S. K., Van Bael, A., 2009. The facet method: A hierarchical multilevel modelling scheme for anisotropic convex plastic potentials. Int. J. Plast. 25 (2), 332–360.

Wang, Z. Q., Beyerlein, I. J., LeSar, R., 2008. Plastic anisotropy in fcc single crystals in high rate deformation. Int. J. Plast. 25 (1), 26–48.